A mixed stress-strain driven computational homogenization of spiral strands

Mohammad Ali Saadat, Damien Durville

Computers and Structures 279 (2023) 106981

Contents lists available at ScienceDirect

Computers and Structures

journal homepage: www.elsevier.com/locate/compstruc

A mixed stress-strain driven computational homogenization of spiral strands

Mohammad Ali Saadat *, Damien Durville

Université Paris-Saclay, CentraleSupélec, ENS Paris-Saclay, CNRS, LMPS - Laboratoire de Mécanique Paris-Saclay, 3 rue Joliot-Curie, Gif-sur-Yvette 91190, France

ARTICLE INFO

Article history:
Received 25 October 2022
Accepted 19 January 2023

Keywords:
Computational homogenization
Spiral strands
Mixed stress-strain driven homogenization
Offline homogenization
Nonlinear hysteretic bending response
Frictional contact interaction

ABSTRACT

Spiral strands subjected to tensile force and bending loading display a nonlinear dissipative behavior due to frictional interactions between their elementary wires. This study aims to provide an efficient method, based on a computational homogenization procedure, to accurately characterize the nonlinear response of such strands. By using 1D beam elements in both micro- and macro-scale, homogenization is performed along the axial direction of a representative volume element (RVE), leading to expressing a boundary value problem on RVE, driven in a mixed manner by either strains or resulting forces or moments. The boundary value problem on the RVE is solved using an in–house implicit finite element solver for finite strain, considering all frictional contact interactions. A method is proposed to predict the bending moment's evolution for any curvature variation from the simulation results of only one bending loading test on the RVE. The nonlinear behavior of the strand in the micro-scale identified through this offline technique can then be used in the macro-model to simulate various bending loading tests under constant tensile load. Results obtained with the multiscale model are compared to those provided by direct numerical simulation to demonstrate the validity of the proposed approach.

1. Introduction

A spiral strand is a multi-layer cable with a helical geometry made of metallic wires with a circular cross-section twisted around a core wire. The cross-section and side view of a typical spiral strand with three layers and a core wire with radius R_c are shown in Fig. 1. The lay angle α_i or the pitch length, the helix radius ρ_i, the wire radius R_i, and the number of wires identify the geometry of each layer of a spiral strand. Due to the helical geometry, the spiral strands exhibit axial–torsional coupling and nonlinear bending behavior, even when the wires are linear elastic, due to frictional contact interactions between wires. In order to explain and predict the behavior of these strands, different approaches have been considered in the literature, including analytical, full 3D finite element simulation, 1D finite element simulation using beam elements, and multi-scale simulation.

The analytical approaches could be broadly divided into two categories, namely, semi-continuous and discrete formulations. In semi-continuous formulation, each layer of a spiral strand is replaced with an equivalent continuum medium, while in discrete formulation, each wire is considered individually. Among many contributions to semi-continuous formulation, the work of [1] could be mentioned. In [2,3], the axial–torsional response of spiral strands is investigated using discrete formulation. The effect of lay angle on the axial–torsional response of multi-strand ropes has been investigated in [4]. In [5,6], the structural pattern of multi-strand ropes has been optimized to maximize the axial load-bearing capacity and minimize the torque in the rope. The nonlinear bending behavior of spiral strands, which is their most complex and interesting mechanical property, has been studied in the pioneering work of [7]. In this study, the bending stiffness of spiral strands when subjected to tensile force varies between two extremes: full stick and full slip bending stiffnesses. This theory has been further modified in [8,9]. In [10], a model has been proposed to describe the behavior of spiral strands subjected to tension, torsion and bending. Although these analytical approaches provide helpful insight into the behavior of these cables, they cannot address all the internal nonlinear mechanisms of complex strands. Therefore, using numerical simulations is inevitable.

In [11–16], full 3D finite element simulations have been performed to model the axial response of spiral strands. However, due to the very high computational cost of these simulations, the domain of application of these models is limited to very short samples of small cables. In order to reduce the computational cost of finite element simulations, one could take advantage of the wires'

* Corresponding author.
E-mail address: mohammad-ali.saadat@centralesupelec.fr (M.A. Saadat).

https://doi.org/10.1016/j.compstruc.2023.106981
0045-7949/

Fig. 1. The side view, internal configuration and cross section of a spiral strand.

slenderness and use 1D beam elements instead of 3D solid elements [17–19]. The beam element has been successfully used to represent wires in many applications. However, in the case of spiral strands, not much work has been done. In the extensive literature on finite element simulation of spiral strands, only a few papers have used beam elements [20–24]. Although using beam elements would reduce the computational cost compared to full 3D simulations, modeling large samples of large cables is still out of reach. In this case, computational homogenization becomes an option.

Several attempts have been made to perform homogenization of beam-like structures [25–29,23,30–32]. In [31,32], the authors have proposed a two-dimensional homogenization scheme by reducing the original 3D microscopic problem to a 2D finite element simulation on the cross-section. Due to the dependence of the bending loading on the axial coordinate of the cable, only the axial and torsional loading could be considered in these works. In [25], this dependence has been accounted for, which makes the presented model capable of modeling the bending behavior. Among different studies, the work of [23] could be considered as the only effort to utilize the full capacity of homogenization methods for spiral strands. In this work, the asymptotic homogenization, previously developed in [30] has been extended to consider contact nonlinearities. Using different element types in the micro-scale model, the authors obtain the mechanical behavior of single- and two-layer strands. Although the results have been compared to different analytical approaches, the integration of the proposed micro-sample analysis in an upper-scale model is missing.

The main goal of the current study is to develop a computational homogenization scheme for spiral strands by modifying the conventional homogenization framework. In the computational homogenization technique, a heterogeneous medium is replaced by its equivalent homogeneous medium. In this framework, the constitutive behavior for each integration point of the homogeneous medium (macro-scale model) is extracted from the representative volume element (RVE) attached to that point, where all the heterogeneities are explicitly modeled, while no explicit assumption on the macroscopic constitutive behavior is necessary. A micro-sample is called RVE upon satisfaction of two criteria: first, it should be large enough to represent the heterogeneity's randomness statistically and second, the homogenized properties should be insensitive to the micro-sample size. In conventional homogenization at finite strain, the macro-scale tangent modulus and first Piola-Kirschoff stress are obtained for a given macroscopic deformation gradient. A review of computational homogenization technique is presented in [33]. In the context of cables, the spiral strand is the heterogeneous medium, a single beam is the macro-scale model, and a short length of the spiral strand is the RVE.

As the macro-scale model is a single beam and the mechanical properties in the longitudinal direction are dominant, the homogenization will be performed only in the longitudinal direction, and no averaging condition is considered in the transverse directions. In the proposed framework, two different beam elements are used in the macro- and micro-scales. A kinematically enriched beam element, which has 9 degrees of freedom and is able to capture the deformation of the cross-section, is used in the micro-scale. For the macro-scale model, the geometrically exact beam element, which has 6 degrees of freedom and considers a rigid cross-section, is used. In this study, cables are considered slender structures whose behavior is dominated by axial, torsional, and flexural mechanisms, and shear strains are neglected. However, it should be emphasized that shear is accounted for on the microscopic scale, as it plays a vital role in determining the macroscopic bending behavior of spiral strands. Consequently, the macroscopic strains of interest are an axial extension, a twist, and two bending curvatures. Moreover, a pure strain-driven scheme could not be employed due to the geometric coupling of axial force and bending curvature, which will be fully explained later. Therefore, following [34], a mixed stress–strain driven homogenization framework is developed. In this formulation, the macroscopic strains enter the microscopic boundary value problem (BVP) as "displacement" degrees of freedom, while their conjugate stresses will be their corresponding dual "forces". This allows strain, stress, or mixed stress–strain driven homogenization to be performed straightforwardly. Furthermore, the macroscopic stresses and strains are naturally obtained as the solution to the microscopic BVP, without needing any averaging relation.

Although utilizing a computational homogenization framework reduces the computational cost compared to direct numerical simulation (DNS), where a full-length spiral strand is modeled, the CPU time is still high for simulating long samples of large cables. Generally, in the computational homogenization framework, if the behavior of RVE is not known a priori (in the case of nonlinear RVE behavior, for example), an RVE is attached to each macroscopic integration point. Therefore, a microscopic BVP is solved for every iteration of every loading step of the macro-scale problem to extract the RVE behavior for each macroscopic point. In the literature, this approach is usually referred to as an online or FE^2 homogenization [35]. Consequently, as the macro-scale model's size increases, the computational cost would be very high. In order to remedy this problem, the computational cost of the micro-scale problem should be reduced. Many authors have tried different methods to reduce the computational cost of homogenization by using reduced-order modeling (see [36] for example) or machine learning algorithms (see [37] for example) in the micro-scale, to name a few. In the current study, it will be shown

that the nonlinear axial-bending response is the primary reason the behavior of the RVEs under study could not be known a priori. Therefore, if this behavior is predicted, offline homogenization can be performed, in which instead of assigning an RVE to each macroscopic integration point, the nonlinear RVE response is calculated using a simple algorithm. By using the proposed offline homogenization, the bending behavior of an RVE under a constant axial force for any given curvature history is predicted based on the results of a monotonic axial-bending test. Therefore, the microscopic BVP is solved only once and is used throughout the simulation. This reduces the computational cost of performing the homogenization by several orders of magnitude compared to the DNS, making it possible to perform simulations of very large cables on a laptop while running the DNS on a workstation is simply impossible. It should be mentioned that since DNS using finite element method has already been verified against experimental results in the literature, it suffices only to verify the results of computational homogenization against DNS.

This paper is organized as follows. First, the beam kinematics and contact algorithm in the micro-scale, followed by the macroscale beam kinematics, are introduced. Next, the proposed computational homogenization algorithm will be formulated. The numerical examples section illustrates the robustness of the proposed homogenization scheme in predicting the nonlinear response of different spiral strands and its objectivity with respect to RVE and finite element size. Then, the offline homogenization scheme is introduced, and the results of the multi-scale simulation are verified against DNS. Finally, some concluding remarks are given.

2. Microscopic model

The spiral strands are modeled in the micro-scale as assemblies of wires with frictional contact interactions. A 1D kinematically enriched finite strain beam element, which has 9 degrees of freedom and can capture the cross-section's in-plane deformations, is used to represent each wire. Frictional contact interactions, the only dissipative mechanism considered in the micro-scale, are modeled explicitly in this scale. The detailed description of the approach implemented in the micro-scale could be found in [18].

The mechanical equilibrium of a sample of spiral strand composed of N_w wires is determined through the minimization of the virtual work in the micro-scale, denoted δW^m, combining the contributions of both internal forces in all wires and frictional contact interactions between wires, expressed in the following way:

$$\delta W^m = \sum_{I=1}^{N_w} \delta W^I + \sum_{k=1}^{N_c} \delta W^k_{cf}, \tag{1}$$

where δW^I is the internal virtual work of each wire I, and δW^k_{cf} is the virtual work of frictional contact interactions related to the k-th discrete contact element generated within the assembly of wires. These two terms are clarified in the following paragraphs.

2.1. Beam kinematics

The beam kinematics used to represent the wires in the micro-scale is based on the assumption that every cross-section can be defined in any configuration using three vectors, namely the position of its center and two unconstrained section directors. By considering the initial configuration of the beam to be straight and aligned with the third axis of an orthonormal frame $(\mathbf{O}, \boldsymbol{e}_1, \boldsymbol{e}_2, \boldsymbol{e}_3)$, the position $\boldsymbol{x}$ at any given time t of any particle of the beam identified by its coordinates (ξ_1, ξ_2, ξ_3) in the initial configuration, is obtained using the position of the centroid of the cross-section, $\boldsymbol{r}$, and the two section directors $\boldsymbol{g}_\alpha$, with $\alpha = 1, 2$ (Fig. 2):

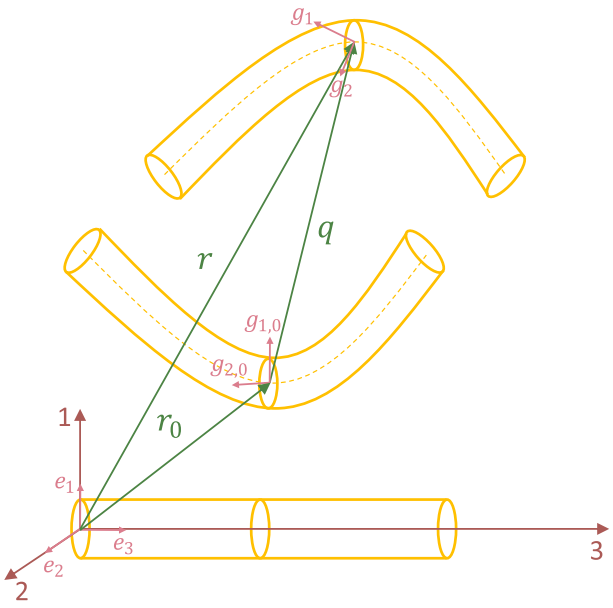

Fig. 2. The beam kinematics in the micro-scale.

$$\boldsymbol{x}(\boldsymbol{\xi}, t) = \boldsymbol{r}(\xi_3, t) + \xi_\alpha \boldsymbol{g}_\alpha(\xi_3, t), \tag{2}$$

where ξ_α are the transverse coordinates of the particle, and ξ_3 is its curvilinear abscissa. Since the two section directors are unconstrained, the beam cross-section can deform, but will remain plane. The displacement $\boldsymbol{u}$ of any particle is obtained by subtracting its initial position, $\boldsymbol{X} = \boldsymbol{x}(\boldsymbol{\xi}, 0)$, from the current position, and is written as follows:

$$\boldsymbol{u}(\boldsymbol{\xi}, t) = \boldsymbol{q}(\xi_3, t) + \xi_\alpha \boldsymbol{h}_\alpha(\xi_3, t), \tag{3}$$

where $\boldsymbol{q}$ is the displacement of the centroid of the cross-section and $\boldsymbol{h}_\alpha$ are the changes of the section directors.

Having the position vector of every particle, the deformation gradient $\mathbf{F}$ can be expressed as

$$\mathbf{F}(\boldsymbol{\xi}) = \frac{d\boldsymbol{x}}{d\boldsymbol{X}}(\boldsymbol{\xi}) = \boldsymbol{g}_\alpha(\xi_3) \otimes \boldsymbol{e}_\alpha + \left(\boldsymbol{r}'(\xi_3) + \xi_\alpha \boldsymbol{g}'_\alpha(\xi_3)\right) \otimes \boldsymbol{e}_3, \tag{4}$$

where $(.)'$ represents differentiation with respect to the curvilinear abscissa. The deformation gradient can be decomposed into a constant part and a linear part with respect to transverse coordinates as:

$$\mathbf{F}(\boldsymbol{\xi}) = \mathbf{F}_0(\xi_3) + \xi_\alpha \mathbf{F}_\alpha(\xi_3). \tag{5}$$

The Green–Lagrange strain tensor $\mathbf{E}$ accordingly expresses as a second order expansion with respect to transverse coordinates:

$$\mathbf{E}(\boldsymbol{\xi}) = \frac{1}{2}\left(\mathbf{F}(\boldsymbol{\xi})^{\mathrm{T}}\mathbf{F}(\boldsymbol{\xi}) - \mathbf{I}\right) = \mathbf{E}_0(\xi_3) + \xi_\alpha \mathbf{E}_\alpha(\xi_3) + \xi_\alpha \xi_\beta \mathbf{E}_{\alpha\beta}(\xi_3), \tag{6}$$

where $\alpha, \beta = 1, 2$, and $\mathbf{I}$ is the second-order identity tensor.

Since no component of the Green–Lagrange strain tensor is a priori zero, because of the planar deformations of cross-sections accounted for through the section directors, a full 3D Hooke's law parameterized by the Lamé coefficients λ and μ can be used. However, since transverse strain terms related to planar deformations of cross-sections are involved only in the zero order tensor $\mathbf{E}_0$, while the traces of higher order tensors $\mathbf{E}_\alpha$ and $\mathbf{E}_{\alpha\beta}$ are constituted only by axial strains, taking into account the traces of these linear and quadratic tensors would generate a Poisson locking. To alleviate this effect, the second Piola-Kirchoff stress tensor $\mathbf{S}$ is expressed as a second order expansion

$$\mathbf{S} = \mathbf{S}_0 + \xi_\alpha \mathbf{S}_\alpha + \xi_\alpha \xi_\beta \mathbf{S}_{\alpha\beta}, \tag{7}$$

each term in this expansion being expressed as a function of the corresponding term of the Green–Lagrange strain tensor expansion (6), using the Hooke's law, but considering the Lamé coefficient λ only for the constant term, as explained in [18]:

$$\mathbf{S}_0 = 2\mu\mathbf{E}_0 + \lambda\mathbf{Tr}(\mathbf{E}_0)\mathbf{I}, \tag{8}$$
$$\mathbf{S}_\alpha = 2\mu\mathbf{E}_\alpha, \tag{9}$$
$$\mathbf{S}_{\alpha\beta} = 2\mu\mathbf{E}_{\alpha\beta}. \tag{10}$$

With the above definition of strains and stresses, the internal virtual work for each wire I is calculated as

$$\delta W^I = \int_{\mathscr{B}_0^I} \mathrm{Tr}(\mathbf{S}\delta\mathbf{E})\mathrm{d}\mathscr{B}, \tag{11}$$

where $\mathscr{B}_0^I$ represents the initial configuration of the wire. In the finite element setting, 3-noded quadratic elements are used for dicretization.

2.2. Frictional contact interactions

Discrete contact elements associating pairs of material particles are used to handle frictional contact interactions occurring between wires in the micro-model. A contact element $\mathscr{E}_c$ is defined by a pair of material particles (ξ^1, ξ^2), located on the surface of two interacting wires, which are predicted to enter into contact. The determination of these contact elements results from a geometrical procedure based on the definition of intermediate geometries associated to proximity zones between wires, as presented in [18]. The determination of contact elements is iterated all along the evolution of the loading to ensure that contact elements are generated at the locations of crossing between wires, even in case of large sliding. The frictional contact interaction force $\boldsymbol{R}_{cf}^k$ developed at the k-th contact element is decomposed into a normal and a tangential part:

$$\boldsymbol{R}_{cf}^k = R_N^k\boldsymbol{n}^k + \boldsymbol{R}_T^k, \tag{12}$$

where $\boldsymbol{n}^k$ is a unit vector defining the normal contact direction for the contact element. R_N^k stands for the normal contact reaction, and $\boldsymbol{R}_T$ for the frictional tangential reaction, both acting on the particles of the contact element.

A regularized penalty is implemented to compute the normal reaction R_N^k as a function of the gap between the particles of the element, defined as

$$\mathrm{gap}(\mathscr{E}_c^k) = \left(\boldsymbol{x}\left(\xi^{k,1}\right) - \boldsymbol{x}\left(\xi^{k,2}\right)\right)\cdot\boldsymbol{n}^k, \tag{13}$$

where $\boldsymbol{x}\left(\xi^{k,i}\right)$ is the current position of the particle $\xi^{k,i}$. A quadratic penalty is considered when the interpenetration is below a regularization threshold p_{reg} as illustrated in Fig. 3. The penalty coefficient k is regularly adjusted for each contact zone so that the maximum interpenetration registered in this contact zone remains lower than a maximum allowed penetration threshold, p_{max}, whose value is taken as 5 times p_{reg}. A regularized Coulomb friction model is used to compute the tangential reaction $\boldsymbol{R}_T$, considering the relative tangential displacement $[\mathbf{u}_T]$ to be reversible as long as its norm does not exceed a threshold denoted $u_{\mathrm{T,rev}}$ (see Fig. 3).

Using the above definitions, the virtual work of frictional contact interactions associated with the k-th contact element, introduced in (1), can be expressed for as:

$$\delta W_{cf}^k = \boldsymbol{R}_{cf}^k\cdot\left(\delta\boldsymbol{x}(\xi^{c,1}) - \delta\boldsymbol{x}(\xi^{c,2})\right). \tag{14}$$

2.3. Non-linear solving

The different non-linearities involved in this model at the micro-scale, which are related to large displacements, contact, and friction, are solved at each step using an iterative algorithm whose details can be found in [18]. This algorithm is used in the present study to carry out simulations firstly on RVEs to characterize their mechanical properties, and secondly on full-length samples, to validate results from the homogenized multi-scale model against direct numerical simulation (DNS).

3. Macroscopic model

A 3D geometrically exact beam element is considered in the macro-scale. The detailed description of the model used in the macro-scale can be found in [38].

3.1. Kinematics

The geometrically exact beam kinematics initially introduced by [17] differs from the one described in the previous section in (2) by considering the beam's cross-sections to remain rigid. In this formulation, the beam is considered to be initially straight. Moreover, the cross-section does not deform during deformation, and therefore its change is described by a rigid body rotation.

In line with the notation used in the previous section, and after considering the above assumptions, the initial configuration of the beam is expressed as (Fig. 4):

$$\boldsymbol{r}_0 = \boldsymbol{r}(\xi_3, 0) = \xi_3\boldsymbol{e}_3, \tag{15}$$
$$\boldsymbol{Y} = \xi_\alpha\boldsymbol{e}_\alpha. \tag{16}$$

The position of any point after deformation is written as:

$$\boldsymbol{x}(\xi_3, t) = \boldsymbol{r}_0 + \boldsymbol{q}(\xi_3, t) + \mathbf{R}(\boldsymbol{\psi}(\xi_3, t))\boldsymbol{Y}, \tag{17}$$

where $\mathbf{R}$ is the rotation describing the current orientation of the cross-section, which is calculated given a vector $\boldsymbol{\psi}$, with the length equal to the amplitude of rotation and the direction of the axis of rotation. By defining the tilde operator, $\tilde{(.)}$, as the skew-symmetric representative of a vector, the rotation matrix is defined in its exponential form as follows:

$$\mathbf{R}(\boldsymbol{\psi}) = \mathbf{I} + \tilde{\boldsymbol{\psi}} + \frac{1}{2!}\tilde{\boldsymbol{\psi}}^2 + \frac{1}{3!}\tilde{\boldsymbol{\psi}}^3 + \ldots. \tag{18}$$

By applying the rotation matrix to the orthonormal frame $(\mathbf{O}, \boldsymbol{e}_1, \boldsymbol{e}_2, \boldsymbol{e}_3)$, the rotated frame $(\mathbf{O}, \boldsymbol{e}_1', \boldsymbol{e}_2', \boldsymbol{e}_3')$ is obtained as:

$$\mathbf{e}_\alpha' = \mathbf{R}\boldsymbol{e}_\alpha, (\alpha = 1, 2, 3). \tag{20}$$

According to this kinematics, the strain of the axial line is defined by the vector

$$\boldsymbol{\Gamma} = \mathbf{R}^T\left(\frac{d\boldsymbol{r}_0}{d\xi_3} - \boldsymbol{e}_1'\right), \tag{21}$$

and the curvature is given by the vector

$$\boldsymbol{K} = \mathbf{T}(\boldsymbol{\psi})\frac{d\boldsymbol{\psi}}{d\xi_3}, \tag{22}$$

where the tangent operator, $\mathbf{T}(\boldsymbol{\psi})$ is defined in its exponential form as:

$$\mathbf{T}(\boldsymbol{\psi}) = \mathbf{I} - \frac{1}{2!}\tilde{\boldsymbol{\psi}} + \frac{1}{3!}\tilde{\boldsymbol{\psi}}^2 + \ldots. \tag{23}$$

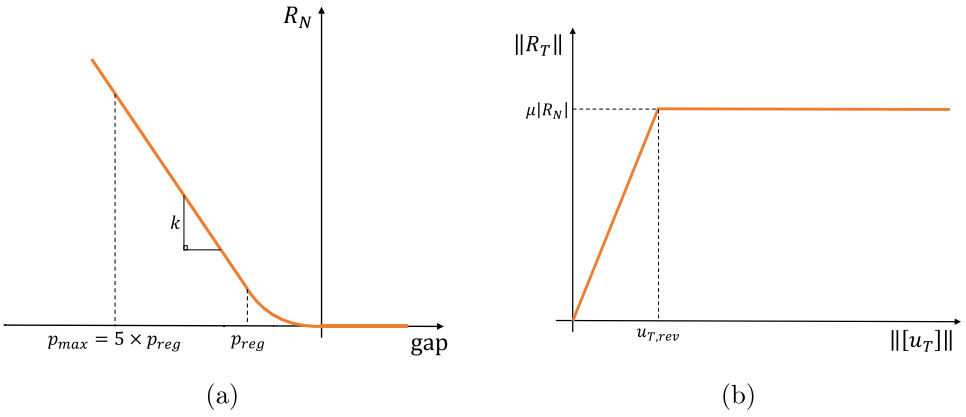

Fig. 3. Models for interactions: a, regularized penalty for normal reaction; b, regularized friction model.

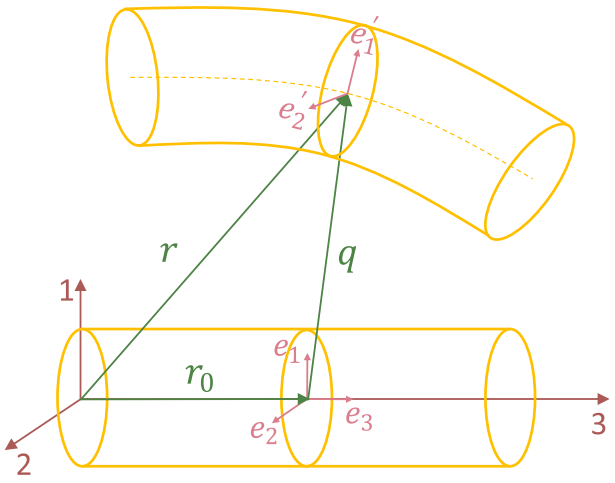

Fig. 4. The beam kinematics in the macro-scale.

3.2. Macro-model virtual work

Following [38], the virtual work for the beam model is expressed as

$$\delta W^M = \boldsymbol{N} \cdot \delta \boldsymbol{\Gamma} + \boldsymbol{M} \cdot \delta \boldsymbol{K}, \tag{24}$$

where $\boldsymbol{N}$ and $\boldsymbol{M}$ correspond respectively to the resulting force and the resulting moment on a cross-section.

Linear 2-noded elements are used for finite element discretization. The beam stress–strain relationship, $\mathbf{C}$, which is a 6×6 matrix, in the case of isotropic elastic behavior of the material, takes the form:

$$\mathbf{C} = diag(EA, GA_1, GA_2, GJ, EI_1, EI_2), \tag{25}$$

where EA is the axial rigidity, GA_1 and GA_2 are shear rigidities along the transverse directions, GJ is the torsional rigidity, and EI_1 and EI_2 are the bending rigidities.

In the following, shear strains and stresses will be assumed to be negligible, and the constitutive model will be derived from the behavior of the micro-model. The only four beam deformation modes retained will be elongation, bending and torsion, handled by the four couples of work-conjugate variables $(\epsilon = \Gamma_3, N = N_3)$, $(K_1, M_1), (K_2, M_2)$, and (K_3, M_3). Using the following notations:

$$\widehat{\boldsymbol{S}}^M = \begin{bmatrix} N \\ M_1 \\ M_2 \\ M_3 \end{bmatrix}; \widehat{\boldsymbol{E}}^M = \begin{bmatrix} \epsilon \\ K_1 \\ K_2 \\ K_3 \end{bmatrix}, \tag{26}$$

the lineic virtual work for the beam model in the macro-scale, restricted to the four deformation modes retained, will be expressed as

$$\delta w^M = \boldsymbol{S}^M \cdot \delta \widehat{\boldsymbol{E}}^M. \tag{27}$$

The homogenization procedure presented in the following will aim at identifying the constitutive behavior of the spiral strand in the macro-scale, by determining the stiffness tensor $\mathbf{C}^M$ and the tangent stiffness tensor $\mathbf{K}_T^M$ used to express the following relationships:

$$\widehat{\boldsymbol{S}}^M = \mathbf{C}^M \widehat{\boldsymbol{E}}^M, \tag{28}$$

$$\delta \widehat{\boldsymbol{S}}^M = \mathbf{K}_T^M \delta \widehat{\boldsymbol{E}}^M. \tag{29}$$

4. Mixed stress–strain driven computational homogenization

In the computational homogenization scheme, the aim is to extract the homogenized material behavior of a heterogeneous medium from micro-scale simulations, in which all heterogeneities are explicitly considered. Since spiral strands are slender, and their mechanical behavior in the longitudinal direction is dominant, beam elements are used in both micro- and macro-scales. The previous sections discuss the kinematics of the beam elements used in the micro- and macro-scales. In order to use beam elements at both scales, homogenization should be performed only in the longitudinal direction. In this manner, the integration in the cross-section of the spiral strand is implicitly considered in the homogenization scheme. Moreover, although shearing effects are fully considered at the micro-scale, both through the beam model for elementary wires and through frictional interactions between wires, shear strains are neglected at the macro-scale. Therefore, the macroscopic strains, $\boldsymbol{E}^M$, are axial strain, ϵ, torsional strain, K_3, and two bending curvatures K_1 and K_2. The macroscopic stresses, $\boldsymbol{S}^M$, are also an axial force, N, torque, M_3, and two bending moments M_1 and M_2.

According to the literature [7,8,10], it is well known that the spiral strands exhibit hysteretic bending behavior due to their internal interwire frictional contact interactions, even when individual wires behave linearly. The presence of external axial tension on a spiral strand causes interlayer normal and, consequently, tan-

gential contact forces. When the cable undergoes bending deformation, interlayer shear forces are developed in the spiral strand. In case these forces are greater than the friction threshold, sliding occurs, causing the bending behavior of spiral strands to be nonlinear. It should be noted that the bending stiffness for these cables depends mainly on axial force. Moreover, a geometric coupling between axial force and bending curvature is observed in large deformation, which will be discussed in detail in the next section.

Due to the dependence of bending stiffness on axial stress and the geometric coupling of axial force and bending curvature, performing a purely strain-driven homogenization, where only the macroscopic strains are imposed on an RVE, is not suitable. Therefore, a mixed stress–strain driven homogenization framework is presented in this study, where the strains or stresses describing the macroscopic mechanical state are considered as input variables of a microscopic BVP, while their work-conjugate quantities are provided as output results. A schematic representation of the proposed computational homogenization scheme is shown in Fig. 5. In the proposed scheme, the macroscopic strains enter into the microscopic BVP as independent "*displacement*" degrees of freedom, while the stresses would be their corresponding "*forces*". The degrees of freedom corresponding to macroscopic strains and their associated resultant forces and moments are treated as conventional displacement and forces in the finite element setting. It should be highlighted that in the mixed strain–stress driven formulation, in contrast to conventional homogenization, where the macroscopic stresses are obtained by averaging the microscopic stresses, the unknown macroscopic parameters are obtained naturally after solving the microscopic BVP.

In the remainder of this section, $(.)^m$ and $(.)^M$ represent variables in the micro-scale and macro-scale domains, respectively.

4.1. Microscopic deformation field

The current position of any particle in the micro-scale domain, could be decomposed into a part caused by the macroscopic deformation, $\boldsymbol{x}_M^m$, and a fluctuation part, $\boldsymbol{w}$, which accounts for heterogenities of the micro-scale, as:

$$\boldsymbol{x}^m = \boldsymbol{x}_M^m + \boldsymbol{w}. \tag{30}$$

Regarding the homogenization procedure, the macroscopic gradient $\boldsymbol{F}^M$ is assumed to be constant with respect to the curvilinear abscissa and to depend only on transverse coordinates X_α. The condition that the average of the microscopic longitudinal gradient over the considered RVE should be equal to the macroscopic longitudinal gradient, $\boldsymbol{F}_3^M$, is then expressed as:

$$\boldsymbol{F}_3^M = \frac{1}{V_{\text{rve}}} \int_{V_{\text{rve}}} \frac{\partial \boldsymbol{x}^m}{\partial X_3} dV, \tag{31}$$

where V_{rve} is the RVE volume. Injecting (30) in (31) we then have

$$\boldsymbol{F}_3^M = \frac{1}{V_{\text{rve}}} \int_{V_{\text{rve}}} \left(\frac{\partial \boldsymbol{x}_M^m}{\partial X_3} + \frac{\partial \boldsymbol{w}}{\partial X_3} \right) dV, \tag{32}$$

and thus

$$\int_{V_{\text{rve}}} \frac{\partial \boldsymbol{w}}{\partial X_3} dV = 0. \tag{33}$$

Decomposing the volume integral into a combination of surface and line integrals, we have

$$\int_{V_{\text{rve}}} \frac{\partial \boldsymbol{w}}{\partial X_3} dV = \int_{S_{\text{rve}}} \left(\int_{L_{\text{rve}}} \frac{\partial \boldsymbol{w}}{\partial X_3} dX_3 \right) dS, \tag{34}$$

where S_{rve} is the cross-section of the macroscopic beam. Assuming this cross-section is constant along the RVE, we can write

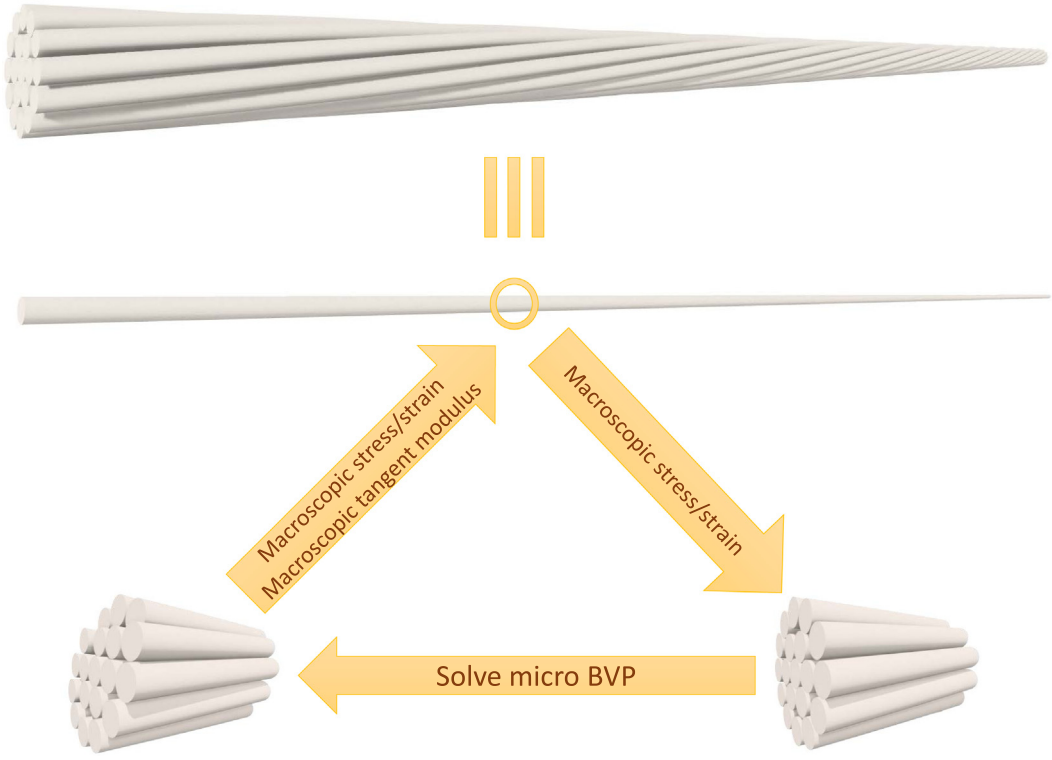

Fig. 5. The computational homogenization algorithm for spiral strands. BVP, boundary value problem.

$$\int_{S_{rve}} \left(\int_{L_{rve}} \frac{\partial \boldsymbol{w}}{\partial X_3} dX_3 \right) dS = \int_{S_{rve}} (\boldsymbol{w}^+ - \boldsymbol{w}^-) dS, \tag{35}$$

where $\boldsymbol{w}^+$ and $\boldsymbol{w}^-$ indicate the fluctuation field on two opposing cross-sections, with X_3^+ and X_3^- as their curvilinear abscissa. From (33), we can therefore conclude that the macroscopic and microscopic gradients have the same average over the RVE if the fluctuation field $\boldsymbol{w}$ satisfies the following condition, which states that the integrals of the fluctuation field over both end sections of the RVE should be equal:

$$\int_{S_{rve}} \boldsymbol{w}^+ dS = \int_{S_{rve}} \boldsymbol{w}^- dS. \tag{36}$$

Among the fluctuations fields which satisfy the previous condition are the periodic fluctuation fields characterized by

$$\boldsymbol{w}^+ = \boldsymbol{w}^-. \tag{37}$$

4.2. Boundary conditions on the borders of the RVE

The averaging conditions expressed above indicate that the fluctuation field should be controlled on both end cross-sections of the beam type RVE. Since the objective is to prescribe the macroscopic deformation gradient to the RVE, we first need to express the displacement field prescribed at the microscopic scale due to the macroscopic deformation gradient.

4.2.1. Microscopic displacement field caused by macroscopic deformation

The deformations of the beam model at the macro-scale are described by the four strain quantities ϵ, K_1, K_2, and K_3. ϵ corresponds to the variation of axial displacement with respect to the abscissa along the beam axis, while other quantities correspond to variations of the rotation. Assuming these variations to be constant along the RVE's beam axis, the macroscopic beam-type displacement field is described by a longitudinal displacement u_3^M and a rotation vector $\boldsymbol{\psi}^M$, both varying linearly with the longitudinal abscissa:

$$u_3^M(X_3) = u_3^M(X_3^-) + (X_3 + L_{rve}) \Delta u_3^M, \tag{38}$$

$$\boldsymbol{\psi}^M(X_3) = \boldsymbol{\psi}^M(X_3^-) + (X_3 + L_{rve}) \Delta \boldsymbol{\psi}^M, \tag{39}$$

where Δu_3^M and $\Delta \boldsymbol{\psi}^M$ denote the variations of the longitudinal displacement and rotation vector per unit length, corresponding to the macroscopic deformations $\boldsymbol{E}^M$. Δu_3^M is simply defined by

$$\Delta u_3^M = \epsilon, \tag{40}$$

while the variation of rotation vector $\Delta \boldsymbol{\psi}^M$ is assumed to be given by:

$$\Delta \boldsymbol{\psi}^M = K_2 \boldsymbol{e}_1 + K_1 \boldsymbol{e}_2 + K_3 \boldsymbol{e}_3. \tag{41}$$

These macroscopic beam-type displacement fields result in both displacement and rotation applied to the enriched beam kinematics adopted at micro-scale to represent the wires in the RVE and defined by the three kinematical vectors $(\boldsymbol{q}, \boldsymbol{h}_1, \boldsymbol{h}_2)$. The macroscopic displacement $\boldsymbol{q}^M$ of a point on the centerline of a wire with coordinates $\boldsymbol{X}$ in the initial configuration results from both u_3^M and $\boldsymbol{\psi}^M$ in the following way:

$$\boldsymbol{q}^M(\boldsymbol{X}) = u_3^M(X_3) + \mathbf{R}(\boldsymbol{\psi}^M(X_3))(X_1 \boldsymbol{e}_1 + X_2 \boldsymbol{e}_2). \tag{42}$$

The variations of section directors due to the macroscopic deformations, denoted $\boldsymbol{h}_\alpha^M$, are assumed to follow the macroscopic rotation and to be defined by

$$\boldsymbol{h}_\alpha^M(\boldsymbol{X}) = \left[\mathbf{R}(\boldsymbol{\psi}^M(X_3)) - \mathbf{I} \right] \boldsymbol{G}_\alpha(X_3), \tag{43}$$

where $\boldsymbol{G}_\alpha = \boldsymbol{g}_\alpha(t=0)$. Finally, the microscopic displacement caused by the macroscopic deformation, $\boldsymbol{u}_M^m$, expressed in terms of the kinematics of the beam model representing the wires at the micro-scale, are obtained. These displacements at all nodes of the discretized model at micro-scale are represented by the vector $\widehat{\boldsymbol{u}}_M^m$ defined as

$$\widehat{\boldsymbol{u}}_M^m = \left[\boldsymbol{q}^{1,M}(i), \boldsymbol{h}_1^{1,M}(i), \boldsymbol{h}_2^{1,M}(i), \ldots, \boldsymbol{q}^{n,M}(i), \boldsymbol{h}_1^{n,M}(i), \boldsymbol{h}_2^{n,M}(i) \right]_{9 \times n}, i = 1,2,3 \tag{44}$$

where $\widehat{(.)}$ indicates the vector form of a variable.

4.2.2. Periodic boundary conditions

The model at micro-scale is defined as a set of wires described using the beam model presented in Section 2. The periodic conditions expressed in (37) should be expressed using the kinematics related to this beam model. The fluctuation field can be expressed as a function of displacement fields as:

$$\boldsymbol{w} = \boldsymbol{u}^m - \boldsymbol{u}_M^m, \tag{45}$$

where $\boldsymbol{u}^m$ is the microscopic beam displacement field, and $\boldsymbol{u}_M^m$ is defined in (44). In the context of spiral strands, due to their helical geometry, each layer i is a periodic structure with a period length l_i^p:

$$l_i^p = \frac{p_i}{n_i}, \tag{46}$$

where p_i and n_i are the pitch length and the number of wires of layer i, respectively.

In case the RVE is periodic, that is, the period lengths of all layers are the same, this period length is considered as the RVE length. In this case, each end of a wire in the left cross-section corresponds to the end of a wire in the opposite right end. Let us denote $\left(N_I^+, N_{J(I)}^-\right)$ a pair of two end nodes of wires associated by these considerations of periodicity, I and $J(I)$ standing for the numbers of the wires associated by periodicity. For this pair of nodes, the periodic condition (37) will express:

$$\boldsymbol{w}(N_I^+) = \boldsymbol{w}\left(N_{J(I)}^-\right). \tag{47}$$

Making use of (45), we obtain the following periodic condition:

$$\boldsymbol{u}^m(N_I^+) - \boldsymbol{u}^m\left(N_{J(I)}^-\right) + \boldsymbol{u}_M^m(N_I^+) - \boldsymbol{u}_M^m\left(N_{J(I)}^-\right) = 0. \tag{48}$$

The conditions expressed for all pairs of wire ends associated by periodicity could be expressed, using the vector form of displacement fields and by means of matrix $\mathbf{A}_p$, in the following way:

$$\mathbf{A}_p(\widehat{\boldsymbol{u}}^m - \widehat{\boldsymbol{u}}_M^m) = 0. \tag{49}$$

4.2.3. Quasi-periodic boundary conditions

Among different options to satisfy the boundary conditions (36), it has been shown that the periodic boundary condition produces reasonable results even for non-periodic RVEs [39].

In the case the RVE is not perfectly periodic, that is, when the period lengths of all layers are not the same, the highest period length is considered as the RVE length, and exact periodic conditions can not be set. In this case, as it can be seen in Fig. 6, the projections of end cross-sections of a generic layer in the $x-y$ plane do not match, and therefore, an angular interpolation is utilized to apply the periodic boundary conditions. If the projection of the first end of wire p is in between the projection of the second end of wires q_1 and q_2, the following relation between their fluctuation field vectors holds:

$$\widehat{\boldsymbol{w}}_p^1 = \frac{\phi_1}{\phi} \widehat{\boldsymbol{w}}_{q_1}^2 + \frac{\phi_2}{\phi} \widehat{\boldsymbol{w}}_{q_2}^2, \tag{50}$$

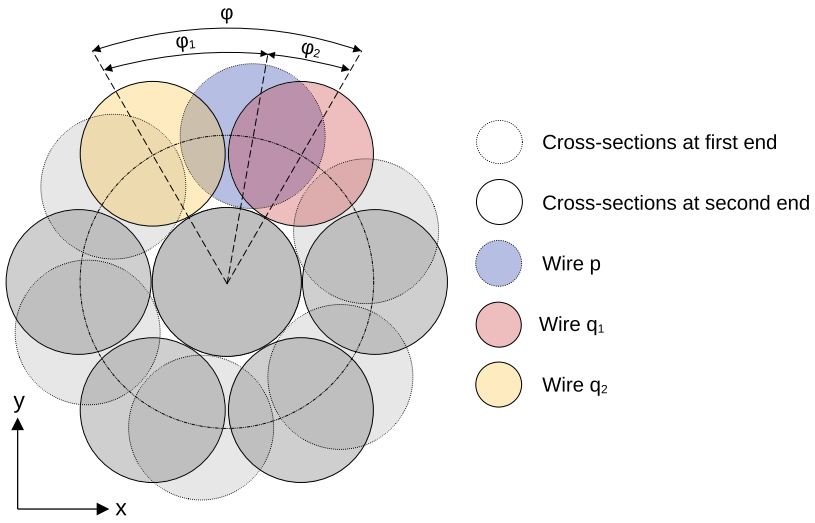

Fig. 6. Representation of periodic boundary conditions for a single-layer non-periodic RVE.

where $\widehat{\boldsymbol{w}}_n^i$ is the 9×1 fluctuation field vector of node n at end i.

It should be noted that from the physical point of view, it makes more sense to perform the interpolation in the polar coordinate system due to the radial symmetry of the strand. However, the interpolation must be performed in the Cartesian coordinate system to satisfy the boundary conditions. Therefore, an error is introduced in the micro-scale solution, which could be significant if the non-periodicity of the RVE is so pronounced. However, if the number of wires in a non-periodic layer is high, the difference between interpolation in the two coordinate systems would be negligible.

Since the boundary conditions only constrain the relative displacement of the opposite faces, rigid body motions are not restricted and should be removed from the solution. To this end, instead of constraining an arbitrary point in the micro-scale domain in all directions, a viscous damping force is added to the equilibrium equation so that the rigid body modes are blocked by viscous dissipation [23].

4.3. Hill-Mandel macrohomogeneity condition

According to the Hill-Mandel condition in its classical form, the variation of work of a macroscopic point, δW^M, should equal the lineic average of δW^m, the variation of work in the RVE. Since homogenization is performed only in one direction in the proposed homogenization scheme, the Hill-Mandel condition should be modified accordingly, that is:

$$\frac{1}{L_{\text{RVE}}}\delta W^m = \delta W^M. \tag{51}$$

4.4. BVP on the RVE

The problem to solve on the RVE is to determine the displacement field at micro-scale $\boldsymbol{u}^m$ satisfying both the boundary conditions (49) and the Hill-Mandel condition (51). Handling periodic conditions by means of Lagrange multipliers arranged into a vector $\widehat{\boldsymbol{\lambda}}$, and defining the macroscopic strain and stress vectors as $\widehat{\boldsymbol{E}}^M = [\epsilon, K_1, K_2, K_3]$ and $\widehat{\boldsymbol{S}}^M = [N, M_1, M_2, M_3]$, respectively, this problem is set in the form of the minimization of the Lagrangian $\mathscr{L}$ defined by:

$$\mathscr{L}\left(\boldsymbol{u}^m, \boldsymbol{\lambda}, \boldsymbol{E}^M\right) = \left(\frac{1}{L_{\text{RVE}}} W^m(\boldsymbol{u}^m) - W^M\left(\boldsymbol{E}^M\right)\right) + \widehat{\boldsymbol{\lambda}}^T \mathbf{A}_P\left(\widehat{\boldsymbol{u}}^m - \widehat{\boldsymbol{u}}_M^m\left(\boldsymbol{E}^M\right)\right). \tag{52}$$

The stationarity conditions with respect to the different variables lead to the equations:

$$\frac{1}{L_{\text{RVE}}}\frac{\partial W^m}{\partial \boldsymbol{u}^m} + \widehat{\boldsymbol{\lambda}}^T \mathbf{A}_P = \mathbf{0}, \tag{53}$$

$$\mathbf{A}_P\left(\widehat{\boldsymbol{u}}^m - \widehat{\boldsymbol{u}}_M^m\right) = \mathbf{0}, \tag{54}$$

$$-\frac{\partial W^M}{\partial \widehat{\boldsymbol{E}}^M} - \widehat{\boldsymbol{\lambda}}^T \mathbf{A}_P \frac{\partial \widehat{\boldsymbol{u}}_M^m}{\partial \widehat{\boldsymbol{E}}^M} = \mathbf{0}. \tag{55}$$

The last condition can be reformulated as

$$\widehat{\boldsymbol{S}}^M = -\widehat{\boldsymbol{\lambda}}^T \mathbf{A}_P \frac{\partial \widehat{\boldsymbol{u}}_M^m}{\partial \widehat{\boldsymbol{E}}^M}. \tag{56}$$

If the homogenization process would be fully strain-driven, the non-linear problem at micro-scale could be solved using only (53) and (54), considering $\left(\boldsymbol{u}^m, \widehat{\boldsymbol{\lambda}}\right)$ as unknown variables, the strains $\widehat{\boldsymbol{E}}^M$ as prescribed quantities, and the macroscopic stresses would be obtained as results through (56). However, to be able to drive the micro-scale boundary-value problem in a mixed way, that is, by prescribing any component of either the macroscopic strains or stresses, the macroscopic strain $\widehat{\boldsymbol{E}}^M$ should be considered as a variable in the non-linear system of equations. Differentiating (53), (54), and (56) and implementing a Newton algorithm, the problem to solve at each iteration is to determine the increments $\left(\delta\boldsymbol{u}^m, \delta\widehat{\boldsymbol{\lambda}}, \delta\widehat{\boldsymbol{E}}^M\right)$ satisfying the following system of equations:

$$\begin{pmatrix} \frac{1}{L_{\text{RVE}}}\frac{\partial^2 W^m}{\partial \boldsymbol{u}^{m2}} & \mathbf{A}_P^T & \mathbf{0} \\ \mathbf{A}_P & \mathbf{0} & -\mathbf{A}_P \frac{\partial \widehat{\boldsymbol{u}}_M^m}{\partial \widehat{\boldsymbol{E}}^M} \\ \mathbf{0} & -\left(\mathbf{A}_P \frac{\partial \widehat{\boldsymbol{u}}_M^m}{\partial \widehat{\boldsymbol{E}}^M}\right)^T & -\widehat{\boldsymbol{\lambda}}^T \mathbf{A}_P \frac{\partial^2 \widehat{\boldsymbol{u}}_M^m}{\partial \widehat{\boldsymbol{E}}^{M2}} \end{pmatrix} \begin{pmatrix} \delta\boldsymbol{u}^m \\ \delta\widehat{\boldsymbol{\lambda}} \\ \delta\widehat{\boldsymbol{E}}^M \end{pmatrix} = \begin{pmatrix} -\frac{1}{L_{\text{RVE}}}\frac{\partial W^m}{\partial \boldsymbol{u}^m} - \widehat{\boldsymbol{\lambda}}^T \mathbf{A}_P \\ -\mathbf{A}_P\left(\widehat{\boldsymbol{u}}^m - \widehat{\boldsymbol{u}}_M^m\right) \\ -\widehat{\boldsymbol{S}}^M + \widehat{\boldsymbol{\lambda}}^T \mathbf{A}_P \frac{\partial \widehat{\boldsymbol{u}}_M^m}{\partial \widehat{\boldsymbol{E}}^M} \end{pmatrix}. \tag{57}$$

In the boundary-value problem, as expressed in (57), the macroscopic strains are treated as "displacement" degrees of freedom, while the macroscopic stresses are their corresponding "forces". Therefore, one could easily impose any set of macroscopic strains or stresses as Dirichlet or Neumann boundary conditions, respectively.

Following [34], the tangent stiffness matrix describing the behaviour of the model at macro-scale can be determined from this formulation, once the convergence of the Newton algorithm is achieved. Differentiating (56) we have

$$\delta\widehat{\boldsymbol{S}}^M = -\delta\widehat{\boldsymbol{\lambda}}^T\mathbf{A}_P\frac{\partial\widehat{\boldsymbol{u}}_M^m}{\partial\widehat{\boldsymbol{E}}^M} - \widehat{\boldsymbol{\lambda}}^T\mathbf{A}_P\frac{\partial^2\widehat{\boldsymbol{u}}_M^m}{\partial\widehat{\boldsymbol{E}}^{M^2}}\delta\widehat{\boldsymbol{E}}^M. \tag{58}$$

At convergence, as the right-hand side in Eq. (57) is assumed to be zero, we can express, using static condensation:

$$\begin{pmatrix}\delta\boldsymbol{u}^m\\ \delta\widehat{\boldsymbol{\lambda}}\end{pmatrix} = \begin{pmatrix}\frac{1}{L_{\text{RVE}}}\frac{\partial^2 W^m}{\partial\boldsymbol{u}^{m2}} & \mathbf{A}_P^T\\ \mathbf{A}_P & \mathbf{0}\end{pmatrix}^{-1}\begin{pmatrix}\mathbf{0}\\ \mathbf{A}_P\frac{\partial\widehat{\boldsymbol{u}}_M^m}{\partial\widehat{\boldsymbol{E}}^M}\end{pmatrix}\delta\widehat{\boldsymbol{E}}^M, \tag{59}$$

and write:

$$\delta\widehat{\boldsymbol{\lambda}}^T\mathbf{A}_P\frac{\partial\widehat{\boldsymbol{u}}_M^m}{\partial\widehat{\boldsymbol{E}}^M} = \left(\mathbf{A}_P\frac{\partial\widehat{\boldsymbol{u}}_M^m}{\partial\widehat{\boldsymbol{E}}^M}\right)^T\delta\widehat{\boldsymbol{\lambda}} \tag{60}$$

$$= \begin{bmatrix}\mathbf{0} & \left(\mathbf{A}_P\frac{\partial\widehat{\boldsymbol{u}}_M^m}{\partial\widehat{\boldsymbol{E}}^M}\right)^T\end{bmatrix}\begin{pmatrix}\delta\boldsymbol{u}^m\\ \delta\widehat{\boldsymbol{\lambda}}\end{pmatrix}. \tag{61}$$

The tangent stiffness matrix of the macro-model $\mathbf{K}_T^M$, such that

$$\delta\widehat{\boldsymbol{S}}^M = \mathbf{K}_T^M\delta\widehat{\boldsymbol{E}}^M, \tag{62}$$

can then be expressed as

$$\mathbf{K}_T^M = \begin{bmatrix}\mathbf{0} & \left(\mathbf{A}_P\frac{\partial\widehat{\boldsymbol{u}}_M^m}{\partial\widehat{\boldsymbol{E}}^M}\right)^T\end{bmatrix}\begin{pmatrix}\frac{1}{L_{\text{RVE}}}\frac{\partial^2 W^m}{\partial\boldsymbol{u}^{m2}} & \mathbf{A}_P^T\\ \mathbf{A}_P & \mathbf{0}\end{pmatrix}^{-1}\begin{pmatrix}\mathbf{0}\\ \mathbf{A}_P\frac{\partial\widehat{\boldsymbol{u}}_M^m}{\partial\widehat{\boldsymbol{E}}^M}\end{pmatrix} - \widehat{\boldsymbol{\lambda}}^T\mathbf{A}_P\frac{\partial^2\widehat{\boldsymbol{u}}_M^m}{\partial\widehat{\boldsymbol{E}}^{M^2}}. \tag{63}$$

As it can be seen, by neglecting shear deformation in the macro-scale, a 4×4 tangent modulus $\mathbf{K}_T^M$ is obtained from Eq. (63) and is inserted into corresponding terms of (25).

It should be noted that all geometric couplings, i.e., the axial–torsional coupling, are explicitly included in (63) and are obtained by solving only one step of homogenization. While the nonlinearities stemming from the presence of frictional contact, e.g., the axial-bending coupling, are implicitly included.

5. Numerical examples

The framework of mixed stress–strain driven homogenization has been developed in the previous sections. In this section, the robustness and capabilities of the proposed homogenization scheme are illustrated using different numerical examples. In the first part of this section, the homogenized responses of different RVEs are investigated. In this part, by considering a single wire as the RVE, the geometric coupling between axial force and bending curvature and the importance of using a mixed stress–strain driven homogenization are highlighted. Next, by introducing more complex RVEs, ranging from a single-layer strand composed of 6 wires to a 6-layer strand composed of 127 wires (see Fig. 7), the nonlinear behavior of the RVEs is investigated. A comparison of the results against different theoretical and numerical results from the literature is also presented. From the studied cases, and within the loading ranges considered, the dependence of the bending moment on both the curvature and the tensile load appears as the main nonlinear mechanism. The objectivity of the proposed homogenization scheme regarding the finite element discretization and RVE size is also investigated in this part. In the second part, the results of the proposed homogenization scheme are verified against those obtained from DNS. First, an offline homogenization scheme is introduced, and it is shown that the cyclic axial-bending response of an RVE for any given curvature history and constant axial force could be predicted using only the results of a monotonic test. Next, by implementing this method, the multi-scale response of different strands under coupled axial force and bending moment is compared to that of the DNS.

In order to study the effect of frictional contact interactions on the bending behavior of spiral strands, it is desirable to consider a case where these interactions are the only dissipative mechanisms. Therefore, although any constitutive behavior could be assumed for each wire, linear elastic behavior is utilized for all wires. In all examples, Young's modulus is 210 GPa, Poisson's ratio is 0.3, and the coefficient of friction is 0.3. The contact regularization parameters, namely the maximum allowed penetration and the reversible tangential displacement, are 10^{-4} mm unless otherwise stated.

5.1. RVE response

5.1.1. Single wire

As the first example, a single wire is considered as the RVE. Although homogenization of a single wire seems trivial, exploring different options and phenomena on a simple RVE is quite helpful. To this end, a wire with a radius of 2.675 mm, with different lengths is considered.

As it has been mentioned earlier, a 3D Hooke's law is used as the constitutive behavior in the micro-scale. Therefore, as the first step, it would be interesting to explore if the homogenized constitutive behavior is, in fact, the beam stiffness of (25). Since the RVE consists of only one wire, the tangent modulus would be diagonal.

The homogenized and analytical tangent moduli are given in Table 1. As it can be seen, by using the proposed homogenization method, one obtains the familiar beam rigidities for a single wire.

Next, the geometric coupling of axial force and bending moment is explored. As depicted in Fig. 8, when a beam is under combined axial force and bending deformation, a secondary moment, $N\delta$, due to the deflection of the beam appears. As this moment has the opposite sign of the applied end moment, it will increase the bending stiffness of the beam, which would be noticeable if the deflection or axial force is high.

In order to examine this effect for a simple single wire case, the response of RVEs with different lengths, namely 10, 50 and 100 mm, under the axial force equivalent to the axial strain of 10^{-3} are compared to the bending stiffness of the wire. The bending moment vs. curvature diagram of these cases is shown in Fig. 9. For a given tension, this secondary moment is proportional to the deflection, which increases both with the prescribed rotation at ends (curvature) and with the length of the sample. As demonstrated in Fig. 9, this secondary moment vanishes if the length is small enough, independently of the curvature.

Finally, the importance of using a mixed stress–strain driven homogenization is highlighted. To this end, the pure bending of the RVE with the length of 100 mm and different macroscopic conditions, namely without axial stress or strain, are investigated. The bending moment vs. curvature diagram for these cases is presented in Fig. 10. As can be observed, to satisfy the zero axial strain condition, an axial force is produced in the cable, which increases the bending stiffness due to the geometric coupling between axial force and bending. The deflected shape of the two cases is depicted in Fig. 10. As it can be seen, the curvature of the beam is not constant in the case of zero axial strain, in contrast to the case with zero axial stress.

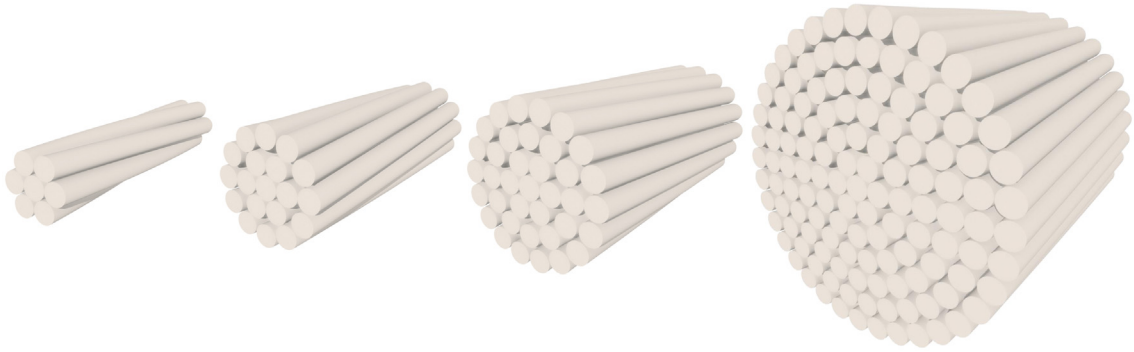

Fig. 7. The representative volume elements composed of a core and one, two, three and six layers.

Table 1
Tangent modulus of the single wire RVE.

Model	EA[kN]	GJ [kN · mm^2]	EI_1 [kN · mm^2]	EI_2 [kN · mm^2]
Analytical	4720.8	6496.2	8445.1	8445.1
Homogenization	4720.8	6496.2	8445.1	8445.1

Fig. 8. The geometric coupling of axial force and bending curvature.

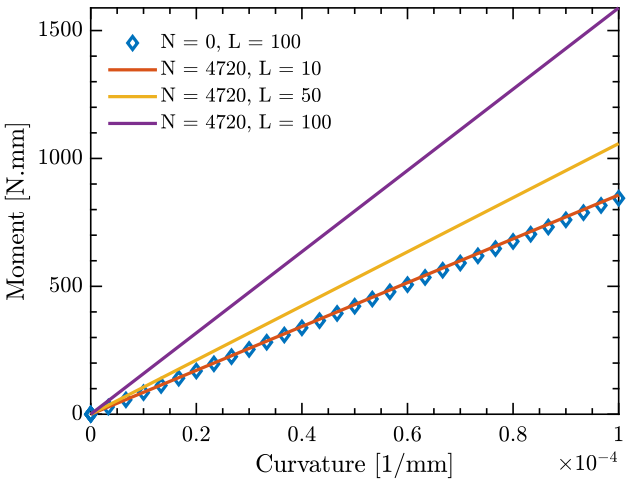

Fig. 9. The response of the single wire RVE with different lengths under combined axial force and bending. The value of axial force is in N.

5.1.2. 1-layer strand

To further investigate the proposed homogenization scheme, a single-layer strand composed of a core wire and six helical wires in the first layer, which has been studied by [23], is analyzed. The geometry of the strand is presented in Table 2. The length of the RVE, i.e., the period of the strand, is $230.1/6 = 38.35$ mm.

First, the linear response of the strand is studied. To study the axial–torsional coupling of the strands, two limit cases, namely the fixed end, where the twist at the ends is fixed, and the free end, where the twist at one end is free, are usually considered. The axial force vs. strain and axial force vs. torque of the strand with the fixed end assumption is compared to the numerical and analytical results presented in [23]. As it can be observed in Fig. 11, the different results are in perfect agreement. It should be noted that, as in the case of axial loading, the frictional contact does not play an important role, the response of the strand could be considered as linear elastic, and therefore, using the homogenized tangent modulus of the strand and static condensation, the response of the strand for the case of free end is obtained as:

$$\begin{bmatrix} \mathbb{C}_{\epsilon\epsilon} & \mathbb{C}_{\epsilon K_3} \\ \mathbb{C}_{K_3\epsilon} & \mathbb{C}_{K_3K_3} \end{bmatrix} \begin{bmatrix} \delta\epsilon \\ \delta K_3 \end{bmatrix} = \begin{bmatrix} \delta N \\ 0 \end{bmatrix} \rightarrow \left(\mathbb{C}_{\epsilon\epsilon} - \frac{\mathbb{C}_{\epsilon K_3}\mathbb{C}_{K_3\epsilon}}{\mathbb{C}_{K_3K_3}} \right) \delta\epsilon = \delta N. \tag{64}$$

The torsional response and also the free bending response of the RVE are also shown in Fig. 12. Again, a very good agreement between the current simulation results and other numerical and analytical solutions is observed.

In order to assess the internal nonlinear mechanisms of the RVE, the inter-wire frictional contact interaction, and its effect on the behavior of the cable, a bending experiment with an axial force is performed. To this end, the cable is subjected to an axial strain of 10^{-3}, and a bending curvature of 10^{-4} mm^{-1} is applied to the RVE while maintaining the axial force constant. The moment vs. curvature diagram of the RVE is presented in Fig. 13. As it can be seen, the result obtained from the proposed homogenization scheme is in very good agreement with the results of the literature. As is expected from spiral strands, the bending behavior under existing axial force is nonlinear. At first, all wires are in sticking condition due to the high contact force and low curvature, and the stiffness is very high. As the bending curvature increases, the wires start sliding, and their contribution to the overall bending stiffness of the strand reduces until the minimum bending stiffness is reached. The slightly higher minimum bending stiffness observed in Fig. 13 is attributed to the geometric coupling of axial force and bending curvature; since referring to Fig. 12, it can be observed that the minimum bending stiffness, which is the stiff-

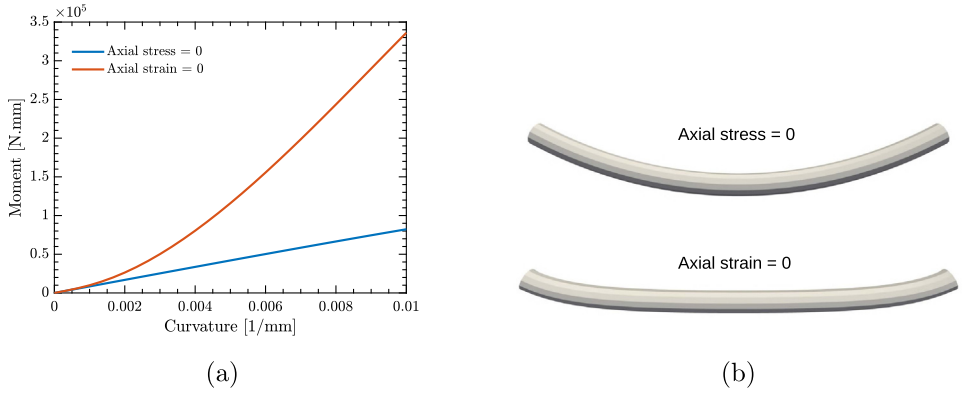

Fig. 10. The bending response of the single wire RVE with zero axial strain or stress. a, Moment vs. curvature diagram; b, Deformed configuration.

Table 2
Geometric properties of the single-layer strand.

	No. of wires	Radius [mm]	Pitch length [mm]
Core	1	2.675	-
Layer 1	6	2.590	230.1

ness without the presence of axial force, has been predicted correctly.

As strands' behavior heavily depends on the contact interactions, both normal and tangential, the effect of different model parameters is explored. First, the effect of the maximum allowed penetration for normal contact, used to adjust the penalty coefficient for each contact zone, will be assessed. The response of the RVE using various maximum allowed penetrations under axial strain is shown in Fig. 14. As it can be observed, the final axial stiffness for all values is the same, but if a large parameter is used, the initial axial stiffness would be lower, as some force would contribute to the initial settlement of wires. In order to examine the effect of the regularization parameter for the tangential contact, the reversible tangential displacement, the bending behavior of the RVE under combined bending and axial load will be studied. As it can be observed in Fig. 14, increasing the reversible relative tangential displacement would decrease the initial stiffness of the friction law and, consequently, the initial bending stiffness of the strand.

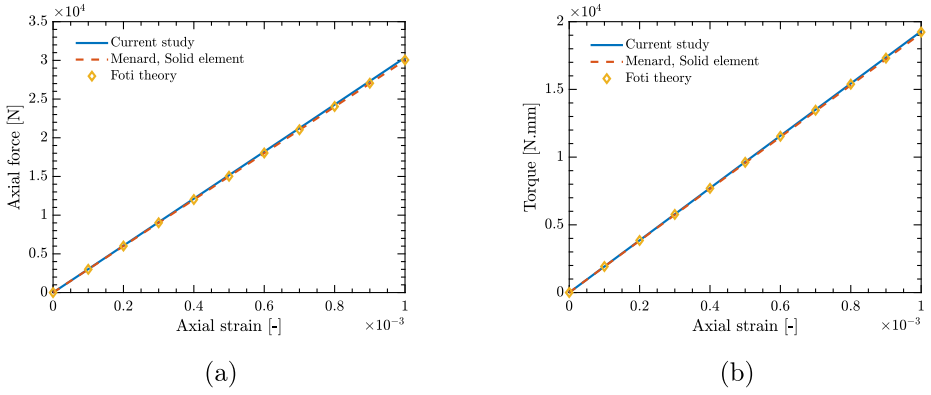

Fig. 11. The axial–torsional response of the single-layer strand. a, Axial force vs. strain diagram; b, Axial torque vs. strain diagram.

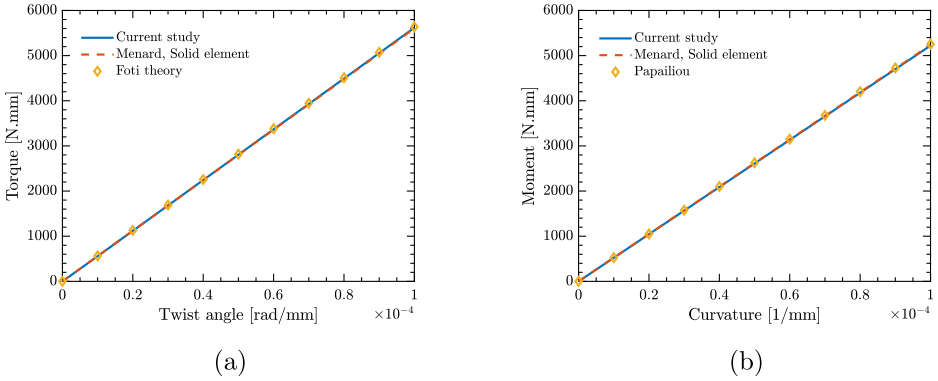

Fig. 12. The torsional and free bending responses of the single-layer strand. a, The torsional behavior; b, The bending behavior.

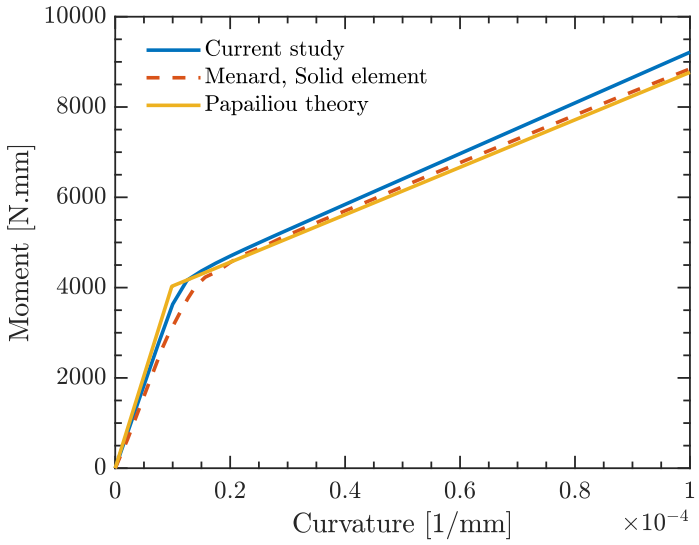

Fig. 13. The behavior of the single-layer strand under combined axial force and bending curvature loading.

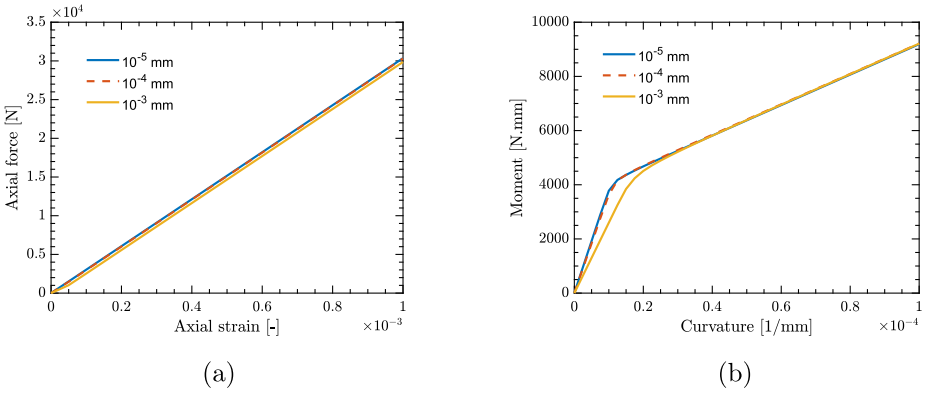

Fig. 14. The effect of contact regularization parameters on the response of the single-layer strand. a, The effect of maximum allowed penetration on the axial response; b, The effect of reversible tangential displacement on the axial-bending response.

5.1.3. 2-layer strand

As the next example, a more complex RVE, a spiral strand with a core wire and two helical layers, is considered. The geometry of the strand is given in Table 3, considering $i = 2$. Since the layer period of both layers is $230.1/6 = 460.2/12 = 38.35$ mm, this length is chosen as the length of the RVE. A comparison of the axial–torsional response of the RVE with fixed ends with analytical and numerical results obtained from the literature is given in Fig. 15, which shows a very good level of agreement. Moreover, the contour of the axial stress over the RVE is also presented in Fig. 16. The effect of contact points on the local stress distribution of the wires and also the periodic pattern of the stress is observed.

To investigate the nonlinear RVE response due to inter-wire frictional interactions, the 2-layer RVE is subjected to an axial force equivalent to an axial strain of 10^{-3} and is then subjected to a bending curvature. The response of the RVE is presented in Fig. 17. As it can be observed, the response is in very good agreement with the results from the literature.

Table 3
Geometric properties of the *i*-layer strand.

	No. of wires	Radius [mm]	Pitch length [mm]
Core	1	2.675	-
Layer *i*	$6 \times i$	2.590	$228.44 \times i$

As it can be seen, the RVE response could be divided into several stages. The contact forces are high enough to avoid sliding at low curvatures, and the bending stiffness is very high. As the curvature increases, the wires of the outermost layer start sliding until all the wires in that layer are sliding, and a drop in the bending stiffness of the strand is observed. Finally, upon further increase in the curvature, the wires in the innermost layer start sliding, and the bending stiffness reaches its minimum value. In Fig. 18, the contour of the axial stress caused by bending at different stages is shown. For small curvatures, all the wires above the middle line are in compression (shown by blue color), and the ones below are in tension (shown by red color), which indicates the wires are bending around the cross-section's middle line. As the curvature grows, wires in the second layer bend around their own middle line, while the wires in the first layer still bend around the cross-section's middle line. Finally, all wires act individually, and individual bending stress patterns are visible for each wire.

The response of RVE under a cyclic bending curvature with an amplitude of 2.10^{-4}mm^{-1} is also depicted in Fig. 19.

5.1.4. 3-layer strand

In order to investigate the effect of the non-periodicity of RVE on its behavior, two 3-layer strands consisting of 37 wires, with and without periodic structure, are considered. The geometry of

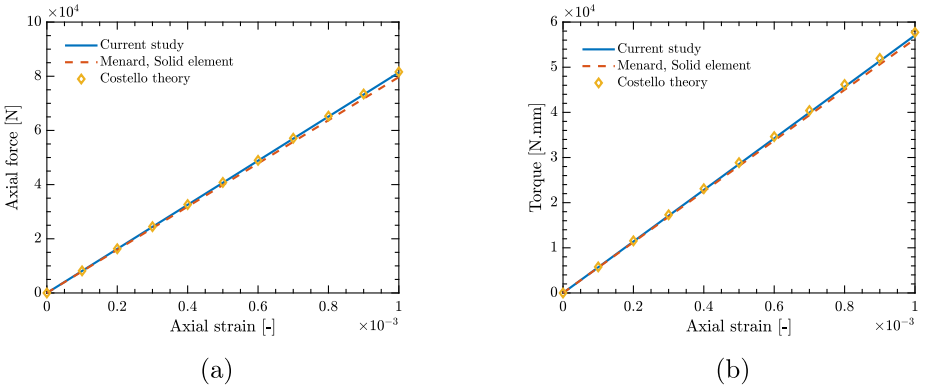

Fig. 15. The axial–torsional response of the 2-layer strand. a, Axial strain vs. axial force diagram; b, Axial strain vs. torque diagram.

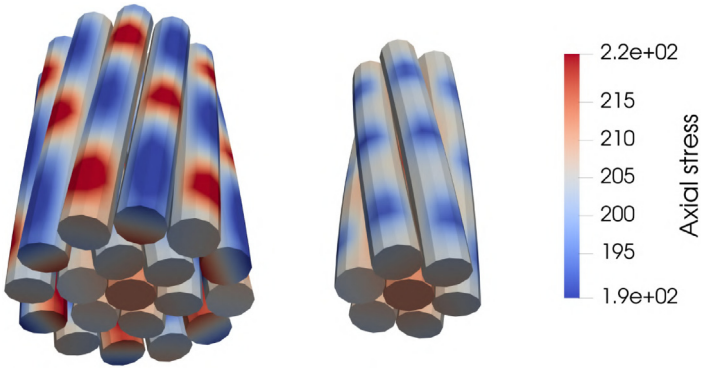

Fig. 16. The axial stress (MPa) contour of the 2-layer strand under tensile strain.

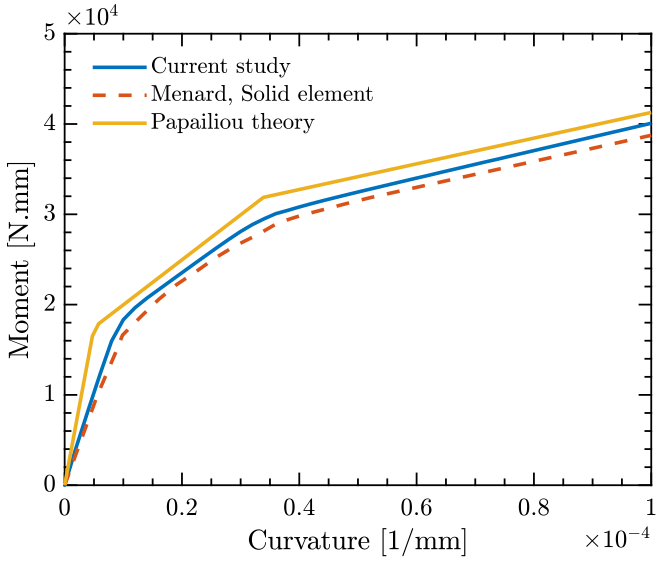

Fig. 17. The 2-layer strand behavior under combined axial force and bending curvature loading.

the non-periodic strand is given in Table 4, while the values of Table 3 with $i = 3$ are used for the periodic RVE. The length of the periodic and non-periodic RVEs is 3.81 mm and 4.0 mm, respectively. The contact regularization parameters are set equal to 10^{-3} mm. Higher bending stiffness is expected for the non-periodic RVE, as its third and second layer's pitch length is lower than the periodic RVE. Table 5.

A comparison of the moment vs. curvature response under combined axial force and bending curvature of both RVEs is given in Fig. 20. For both RVEs, the four lines depicting different sliding stages could be distinguished, and the higher bending stiffness of the non-periodic RVE is noticeable, especially in the region corresponding to the sliding of the outermost layer of both RVEs.

5.1.5. 6-layer strands

As the last example of this part, to show the effectiveness of the proposed homogenization scheme and the contact algorithm used in the micro-scale domain, a 6-layer strand composed of 127 wires is considered as the RVE. The axial-bending response, considering 10^{-3} mm for the regularization parameters, is shown in Fig. 21. As the considered spiral strand has six layers, seven lines corresponding to the sliding of different layers can be distinguished. These lines are identified in Fig. 21 by zooming on different intervals of the moment–curvature diagram.

5.1.6. Objectivity of the proposed homogenization scheme

In this section, the objectivity of the proposed homogenization scheme with respect to the finite element discretization and RVE size is investigated.

First, the axial tension and combined axial tension and bending curvature experiments are performed on the single-layer RVE with various elements per wire to show objectivity with respect to the finite element discretization. As it can be seen from Fig. 22, the results are independent of the micro-scale problem's discretization.

In order to evaluate the objectivity with respect to the RVE size, different sizes of the single-layer RVE, with 1, 2, and 3 periods are considered, and the axial tension, bending, and coupled axial ten-

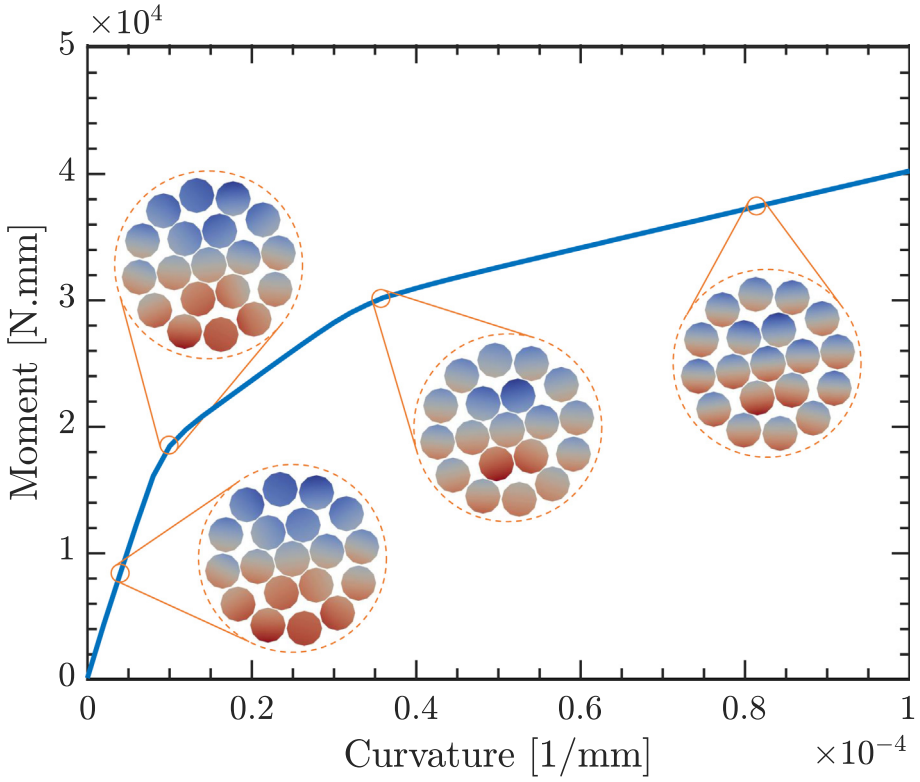

Fig. 18. The contour of axial bending stress of the 2-layer strand under combined axial force and bending curvature loading. For each cross-section, the values have been normalized with respect to the maximum tensile, shown in red, and compressive stresses, shown in blue.

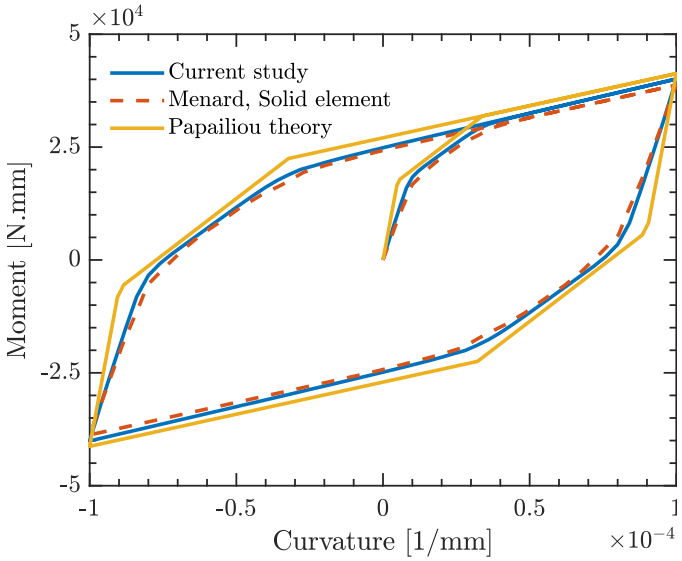

Fig. 19. The 2-layer strand behavior under combined axial force and cyclic bending curvature loading.

Table 4
Geometric properties of the non-periodic 3-layer strand.

	No. of wires	Radius [mm]	Pitch length [mm]
Core	1	2.675	-
Layer 1	6	2.590	228.44
Layer 2	12	2.590	−479.72
Layer 3	18	2.590	639.63

sion and bending moment experiments are performed. The results for the tensile and bending cases are depicted in Fig. 23. Obviously, the tensile and bending experiments are independent of the RVE size. However, a size dependence is observed for the coupled axial tension and bending experiment, as observed in Fig. 24. This difference, which is attributed to the geometric coupling of axial tension and bending curvature, has already been discussed for a single-wire RVE. However, as the cable becomes larger and larger, the dependence would be less pronounced. As it can be seen, increasing the size of RVE for a periodic 3-layer cable does not change the behavior as much as it would for the single-layer RVE. Generally, choosing the smallest possible RVE size is always preferable, as the computational cost and the effect of geometric coupling of axial tension and bending curvature will be minimal.

5.2. Verification of the homogenization scheme

In this section, the results of the multi-scale analysis are verified against direct numerical simulation (DNS) carried out using the micro-model introduced in Section 2 on full-length samples. The geometry and boundary conditions of a bending experiment under constant axial force are shown in Fig. 25. In order to satisfy the separation of scales, $L/4$ is considered equal to two pitches of the outermost layer.

In the examples presented above, and within the loading ranges considered, examining the tangent stiffness matrices identified on RVEs (63), it has been noted that extra-diagonal terms can be considered as negligible, and that stiffness terms remain almost constant, except the bending stiffness terms which displays the main non-linearities. Therefore, instead of performing a FE^2 homogenization method, which would be computationally intensive, an offline homogenization framework is employed, in which, assum-

Table 5
Algorithm for offline prediction of the moment vs. curvature response of an RVE.

Initialization $K_{max} = 0, K_{dir} = 0, dir = 0$
For each time step n
$dK = K_n - K_{n-1}$
if $sign(dK) \neq dir$
  dir = $sign(dK)$
  $K_{dir} = K_{n-1}$
  if $|K_{n-1}| > |K_{max}|$
    $K_{max} = K_{n-1}$
  end if
end if
if $|K_n| > |K_{max}|$
  $dM = dir\left(\mathbb{M}_{K_n} - \mathbb{M}_{K_{n-1}}\right)$
else
  $dM = 2dir\left(\mathbb{M}_{0.5|K_{dir}-K_n|} - \mathbb{M}_{0.5|K_{dir}-K_{n-1}|}\right)$
end if

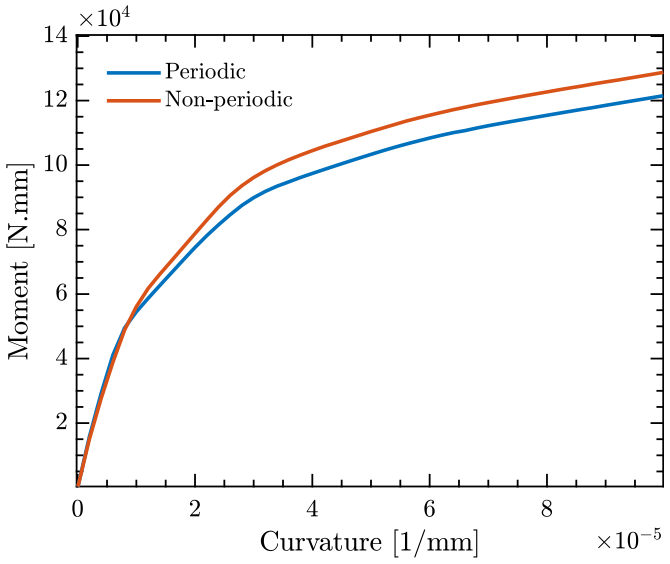

Fig. 20. The periodic and non-periodic 3-layer strands behavior under combined axial force and bending curvature loading.

ing the bending occurs only about one axis (uniaxial bending), the bending response of the RVE is predicted numerically for any strain history, using only the first loading curve of the moment vs. curvature diagram. This offline identification reduces drastically the computation cost compared to a FE^2 approach.

5.2.1. Offline homogenization scheme

In the offline homogenization scheme, instead of imposing the macroscopic variables to an RVE and solving the microscopic BVP to obtain the unknown macroscopic variables (Fig. 5), the microscopic response, namely the moment vs. curvature, is predicted based on the results of a monotonic test. To predict the response of an RVE, a straightforward algorithm with negligible error, even in the case of large loading steps, is used, which is given below.

In this algorithm, K_{max}, K_{dir}, and dir are history variables, dK is the curvature increment, K_n is the curvature at step n, and $\mathbb{M}_K$ is the corresponding moment in the first loading of a given curvature K, which is obtained using cubic-spline interpolation. In order to illustrate the performance of the proposed algorithm, the response of the 2-layer strand under cyclic loading with variable amplitude is shown in Fig. 26. Although only the first loading curve (Fig. 20) has been used as an input, the response has been predicted accurately.

5.2.2. Comparison against DNS

As the first example, the single-layer strand is considered. The moment vs. curvature diagram in Fig. 17 is used as the input for the RVE response predictor algorithm. The force vs. displacement diagram of the multi-scale and DNS models is presented in Fig. 27, along with the responses considering the strand's theoretical maximum and minimum bending stiffnesses [7]. The maximum bending stiffness is computed as a function of the second moment of area of the strand, assuming its cross-section remains rigid (no sliding), while the minimum bending stiffness is taken equal to the sum of the bending stiffnesses of all constituent wires. As it can be observed, the response of the DNS is perfectly predicted by the multi-scale method. As expected, at low deflections, the response is similar to the case considering the maximum bending stiffness, and the final stiffness is equal to the minimum bending stiffness. The deformed shape and curvature at the end of the loading are also shown in Fig. 28.

In order to explore more complicated microstructures, the 2-layer and the non-periodic 3-layer RVEs are considered as the microstructure of the cable. The force vs. displacement diagrams of the multi-scale and DNS models are presented in Fig. 29, considering 10^{-3} mm as the contact regularization parameters. This comparison against DNS for the non-periodic RVE, shows the

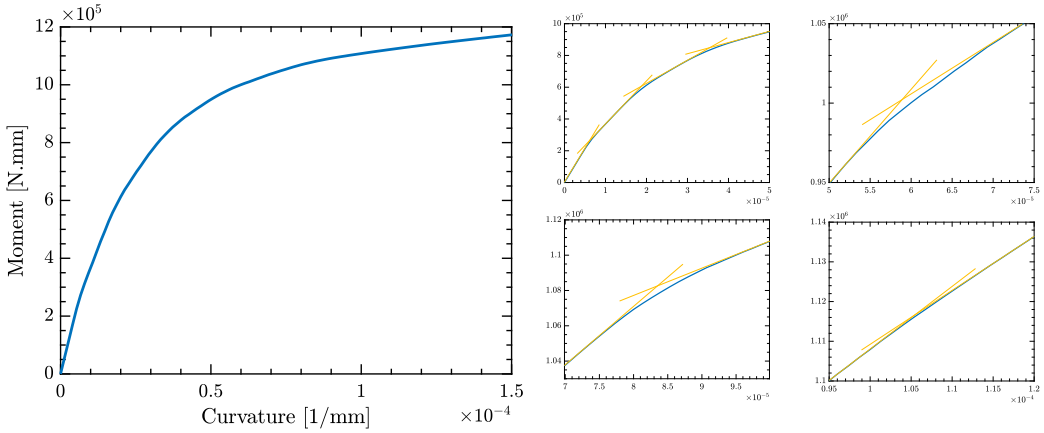

Fig. 21. The 6-layer strand behavior under combined axial force and bending curvature loading, along with identification of different lines corresponding to sliding of different layers.

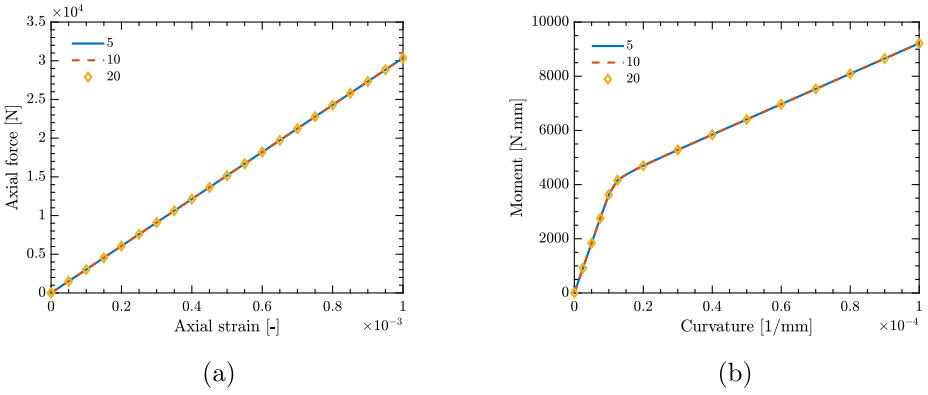

Fig. 22. The effect of finite element discretization on the single-strand RVE behavior. a, The axial behavior; b, The axial-bending behavior.

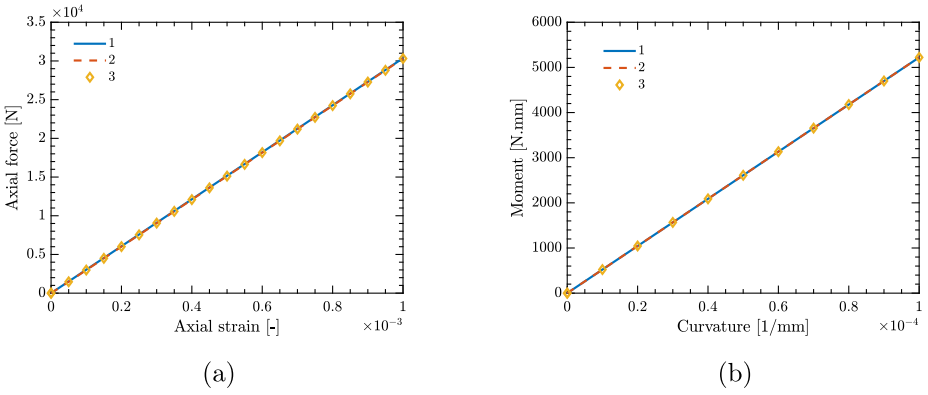

Fig. 23. The effect of RVE size on the single-strand RVE behavior. a, The axial behavior; b, The bending behavior.

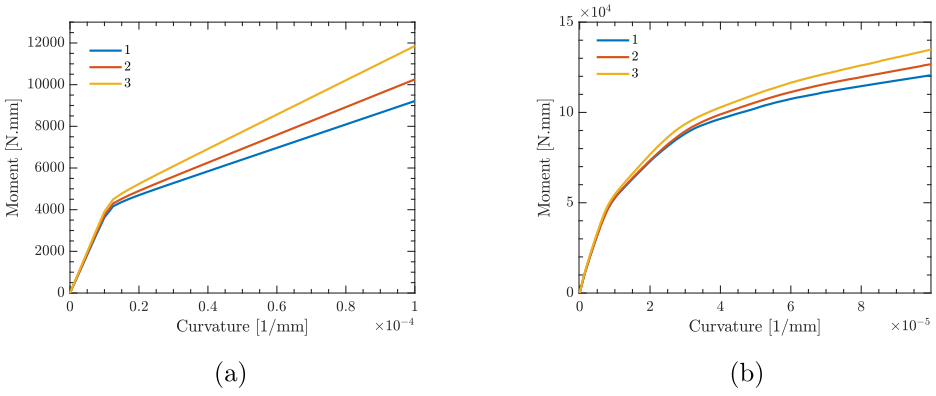

Fig. 24. The effect of RVE size on the axial-bending behavior of different RVEs. a, The single-layer RVE; b, The 3-layer RVE.

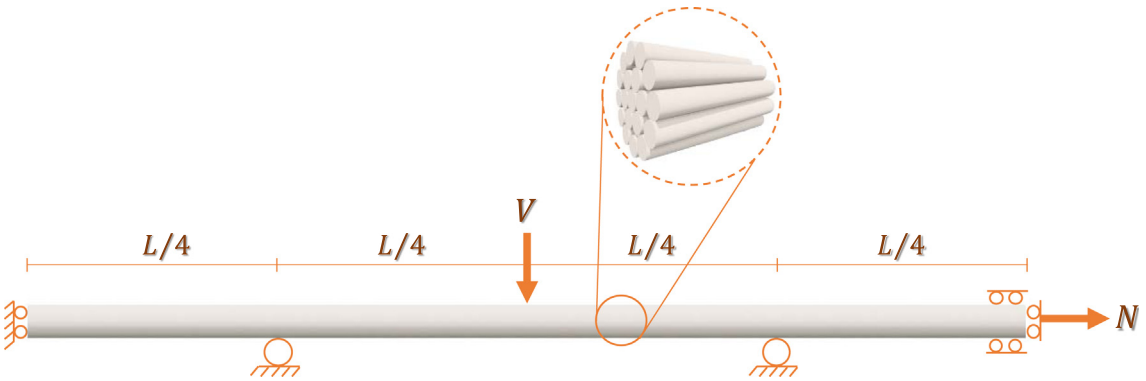

Fig. 25. The geometry and boundary conditions of the bending under constant axial force.

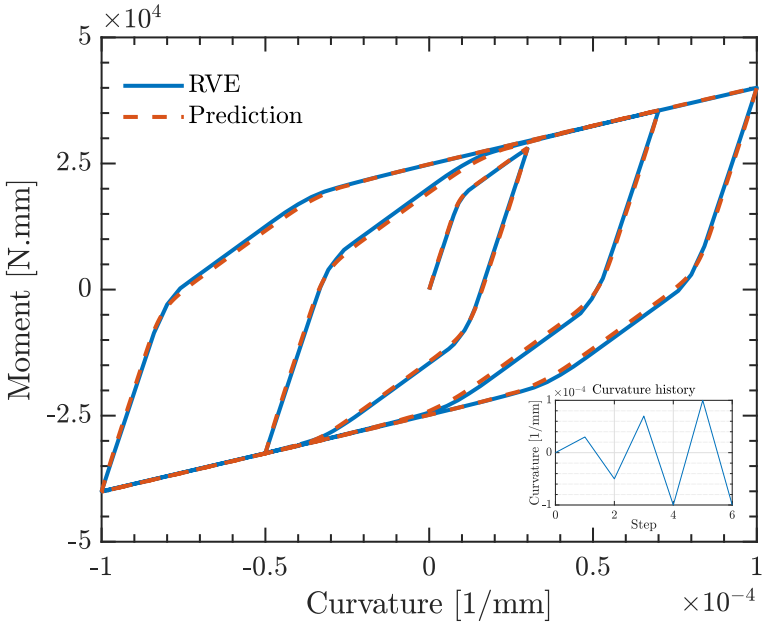

Fig. 26. Comparison of the offline behavior prediction and the actual response of the 2-layer RVE under combined axial force and cyclic bending curvature.

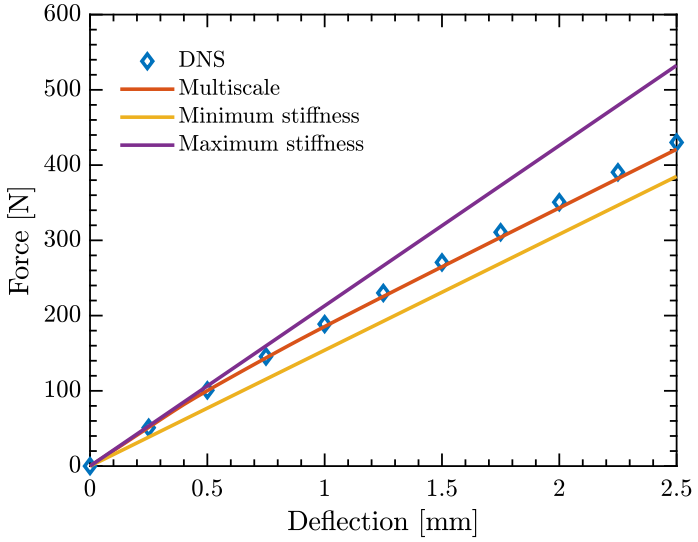

Fig. 27. The force–deflection response of a strand under bending with constant axial force obtained through the DNS, multi-scale analysis, and theoretical stiffnesses, for the single-layer RVE.

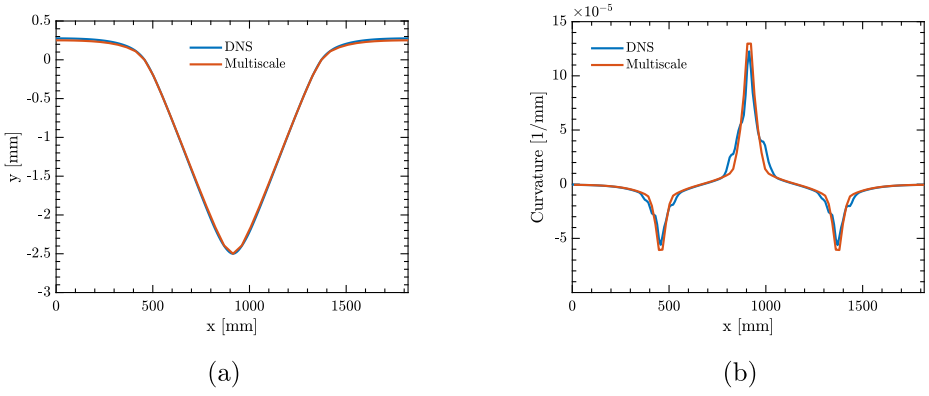

Fig. 28. The response of a strand under bending with constant axial force obtained through the DNS and multi-scale analysis, for the single-layer RVE. a, Deformed configuration; b, Curvature.

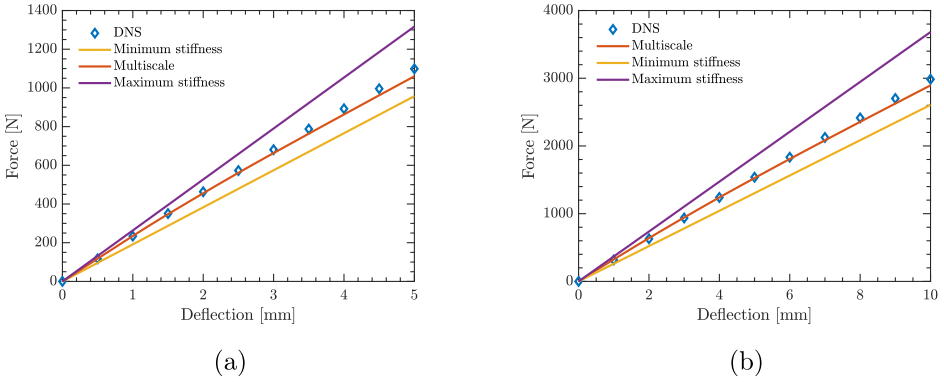

Fig. 29. The force–deflection responses of a strand under bending with constant axial force obtained through the DNS, multi-scale analysis, and theoretical stiffnesses. a, The 2-layer RVE; b, The non-periodic 3-layer RVE.

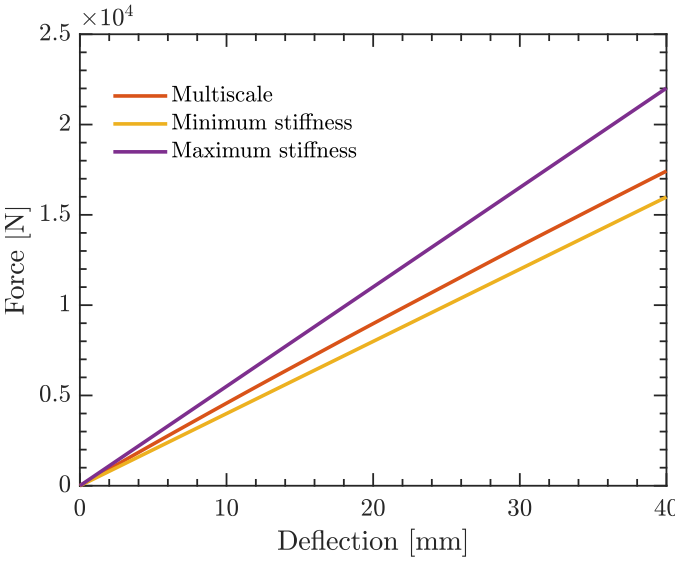

Fig. 30. The force–deflection response of a strand under bending with constant axial force obtained through the DNS, multi-scale analysis, and theoretical stiffnesses, for the 6-layer RVE.

capabilities of the proposed homogenization scheme for non-periodic RVEs. It should be highlighted that for the case of non-periodic 3-layer RVE, the DNS model has been discretized using 29600 quadratic elements (533133 dofs). In contrast, the RVE has been discretized using 740 quadratic elements (13653 dofs) for the multi-scale model, and the macro-scale model has 80 linear elements (486 dofs).

Finally, for the 6-layer RVE, as the DNS model exceeds our available computational capacity, only a comparison against the theoretical minimum and maximum stiffnesses is presented in Fig. 30. It should be noted that this example shows the robustness of the presented offline homogenization scheme, as after obtaining the monotonic response of the RVE, Fig. 21, the multi-scale analysis is carried out on a personal computer in a few seconds, while running the DNS on a supercomputer is not possible.

6. Conclusions

A computational homogenization has been presented in this study to identify the non-linear constitutive model of a beam element able to reproduce the complex hysteretic response of spiral strands subject to bending under tension. Various bending tests on full-length samples of spiral strands can be simulated with high accuracy and at a very low computational cost, thanks to an associated prior offline identification procedure based on a unique monotonic bending simulation performed on an RVE.

Following the choice of a beam model to represent the spiral strand at the macro-scale, the homogenization is performed only in the axial direction, leading to prescribing periodic conditions at both ends of the RVE. Neglecting shear stresses, the local loading at the macro-scale is defined by either resulting force/moment or strain corresponding to elongation, bending, and twisting beam deformation modes. By highlighting a geometric non-linear coupling between axial loading and bending, it has been shown that the BVP on the RVE should be set in a mixed stress–strain form. This way, resulting forces or strains act respectively as forces or displacements is a standard boundary value problem. The BVP at the micro-scale is solved using a non-linear solver, accounting for all wires and frictional contact interactions between them within a large displacement and finite strain framework. It has been shown that periodic boundary conditions could be utilized, even for non-periodic RVEs. Several numerical examples illustrate the robustness of the proposed framework in capturing the mechanical behavior of spiral strands and are compared with results available in the literature. Since the different cases of bending under tension which have been examined showed that stiffness terms could be assumed constant except the bending stiffness demonstrating a non-linear dependence on the curvature, a procedure has been proposed to retrieve the evolution of the bending moment as a function of any curvature history, based on a single monotonic bending test simulation performed on an RVE. Once this prior identification has been carried out, simulations at the macro-scale with the homogenized beam model can be performed at very low computational cost, and excellent agreement is obtained with the results of DNS on the tested configurations.

Data availability

Data will be made available on request.

Declaration of Competing Interest

The authors declare that they have no known competing financial interests or personal relationships that could have appeared to influence the work reported in this paper.

Acknowledgement and disclaimer

This work has received funding from the European Union's Horizon 2020 research and innovation programme under the

Marie Skłodowska-Curie grant agreement No 860124. The present paper only reflects the authors' views. The European Commission and its Research Executive Agency are not responsible for any use that may be made of the information it contains.

References

[1] Raoof M, Hobbs RE. Analysis of multilayered structural strands. J Eng Mech 1988;114:1166–82.
[2] Costello GA. Theory of wire rope. Springer Science & Business Media; 1997.
[3] Foti F, Martinelli L. Modeling the axial-torsional response of metallic strands accounting for the deformability of the internal contact surfaces: derivation of the symmetric stiffness matrix. Int J Solids Struct 2019;171:30–46.
[4] Liu L, Zheng S, Liu D. Effect of lay direction on the mechanical behavior of multi-strand wire ropes. Int J Solids Struct 2020;185:89–103.
[5] Karathanasopoulos N, Angelikopoulos P. Optimal structural arrangements of multilayer helical assemblies. Int J Solids Struct 2016;78:1–8.
[6] Liu L, Liu D, Wu X, He Y. Optimal structural patterns of multi-strand wire ropes. Int J Solids Struct 2021;225:111070.
[7] Papailiou K. On the bending stiffness of transmission line conductors. IEEE Trans Power Deliv 1997;12:1576–88.
[8] Hong K-J, Der Kiureghian A, Sackman JL. Bending behavior of helically wrapped cables. J Eng Mech 2005;131:500–11.
[9] Inagaki K, Ekh J, Zahrai S. Mechanical analysis of second order helical structure in electrical cable. Int J Solids Struct 2007;44:1657–79.
[10] Foti F, Martinelli L. Mechanical modeling of metallic strands subjected to tension, torsion and bending. Int J Solids Struct 2016;91:1–17.
[11] Ghoreishi SR, Messager T, Cartraud P, Davies P. Validity and limitations of linear analytical models for steel wire strands under axial loading, using a 3d fe model. Int J Mech Sci 2007;49:1251–61.
[12] Judge R, Yang Z, Jones S, Beattie G. Full 3d finite element modelling of spiral strand cables. Constr Build Mater 2012;35:452–9.
[13] Frigerio M, Buehlmann P, Buchheim J, Holdsworth SR, Dinser S, Franck CM, et al. Analysis of the tensile response of a stranded conductor using a 3d finite element model. Int J Mech Sci 2016;106:176–83.
[14] Stanova E, Fedorko G, Fabian M, Kmet S. Computer modelling of wire strands and ropes part ii: Finite element-based applications. Adv Eng Softw 2011;42:322–31.
[15] Fekr MR, McClure G, Farzaneh M. Application of adina to stress analysis of an optical ground wire. Comput Struct 1999;72:301–16.
[16] Qi G. Computational modeling for stress analysis of overhead transmission line stranded conductors under design and fretting fatigue conditions. 2014.
[17] Simo JC. A finite strain beam formulation. the three-dimensional dynamic problem. part i. Comput Methods Appl Mech Eng 1985;49:55–70.
[18] Durville D. Contact-friction modeling within elastic beam assemblies: an application to knot tightening. Comput Mech 2012;49:687–707.
[19] Sonneville V, Cardona A, Brüls O. Geometrically exact beam finite element formulated on the special euclidean group se (3). Comput Methods Appl Mech Eng 2014;268:451–74.
[20] Zhou W, Tian H-Q. A novel finite element model for single-layered wire strand. J Central South Univ 2013;20:1767–71.
[21] Lalonde S, Guilbault R, Légeron F. Modeling multilayered wire strands, a strategy based on 3d finite element beam-to-beam contacts-part i: Model formulation and validation. Int J Mech Sci 2017;126:281–96.
[22] Lalonde S, Guilbault R, Langlois S. Modeling multilayered wire strands, a strategy based on 3d finite element beam-to-beam contacts-part ii: Application to wind-induced vibration and fatigue analysis of overhead conductors. Int J Mech Sci 2017;126:297–307.
[23] Ménard F, Cartraud P. Solid and 3d beam finite element models for the nonlinear elastic analysis of helical strands within a computational homogenization framework. Comput Struct 2021;257:106675.
[24] Kim H-J, Lee D-H, Yoon K, Lee P-S. A multi-director continuum beam finite element for efficient analysis of multi-layer strand cables. Comput Struct 2021;256:106621.
[25] Treyssede F, Cartraud P. A two-dimensional formulation for the homogenization of helical beam-like structures under bending loads. Int J Solids Struct 2022;234:111270.
[26] Staszak N, Gajewski T, Garbowski T. Shell-to-beam numerical homogenization of 3d thin-walled perforated beams. Materials 2022;15:1827.
[27] Xing Y, Meng L, Huang Z, Gao Y. A novel efficient prediction method for microscopic stresses of periodic beam-like structures. Aerospace 2022;9:553.
[28] Boso DP, Lefik M, Schrefler BA. A multilevel homogenised model for superconducting strand thermomechanics. Cryogenics 2005;45:259–71.
[29] Buannic N, Cartraud P. Higher-order effective modeling of periodic heterogeneous beams. i. asymptotic expansion method. Int J Solids Struct 2001;38:7139–61.
[30] Cartraud P, Messager T. Computational homogenization of periodic beam-like structures. Int J Solids Struct 2006;43:686–96.
[31] Karathanasopoulos N, Kress G. Two dimensional modeling of helical structures, an application to simple strands. Comput Struct 2016;174:79–84.
[32] Frikha A, Cartraud P, Treyssede F. Mechanical modeling of helical structures accounting for translational invariance. part 1: Static behavior. Int J Solids Struct 2013;50:1373–82.
[33] Geers MG, Kouznetsova VG, Brekelmans W. Multi-scale computational homogenization: Trends and challenges. J Comput Appl Mathe 2010;234:2175–82.
[34] van Dijk NP. Formulation and implementation of stress-driven and/or strain-driven computational homogenization for finite strain. Int J Numer Meth Eng 2016;107:1009–28.
[35] Feyel F, Chaboche J-L. Fe2 multiscale approach for modelling the elastoviscoplastic behaviour of long fibre sic/ti composite materials. Comput Methods Appl Mech Eng 2000;183:309–30.
[36] Zhang X, Oskay C. Eigenstrain based reduced order homogenization for polycrystalline materials. Comput Methods Appl Mech Eng 2015;297:408–36.
[37] Capuano G, Rimoli JJ. Smart finite elements: A novel machine learning application. Comput Methods Appl Mech Eng 2019;345:363–81.
[38] Géradin M, Cardona A. Flexible multibody dynamics: a finite element approach. Wiley; 2001.
[39] Terada K, Hori M, Kyoya T, Kikuchi N. Simulation of the multi-scale convergence in computational homogenization approaches. Int J Solids Struct 2000;37:2285–311.